EXPERIMENTAL AND NUMERICAL INVESTIGATION OF THE DYNAMICS OF INTERACTING VORTEX RINGS IN SUPERFLUID HELIUM

A THESIS SUBMITTED TO THE UNIVERSITY OF MANCHESTER
FOR THE DEGREE OF MASTER OF PHILOSOPHY
IN THE FACULTY OF ENGINEERING AND PHYSICAL SCIENCES

2015

Tianhui Zhu
School of Physics and Astronomy

Contents

Word count $\approx$ 13,000

List of Figures

Abstract

The University of Manchester
Tianhui Zhu
Master of Philosophy
Experimental and Numerical Investigation of
the Dynamics of Interacting Vortex Rings in Superfluid Helium
2015

This thesis focuses on the dynamics of the vortex rings and how they interact with each other in superfluid helium. A pulse of charged vortex rings (CVRs) is injected into the experimental cell for different pulse lengths, voltages and temperatures. It is shown that the properties of the large charged tangle near the injection tip, which releases CVRs by reconnections, present little voltage-dependence or temperature-dependence. In the zero temperature limit, the experimental time of flight agrees with the analytical calculations of an isolated CVR at low drive voltages. At drive voltages above 50 V, reconnections start to occur, which leads to the production of small rings, the wider spread of the radii of the CVRs and the change of dominant charge carriers to charged vortex tangles. At finite temperatures, when mutual friction cannot be ignored, many of the CVRs are dissipated before reaching the collector on the other side of the cell.

The interactions between a pair of vortex rings, both circular and deformed, have been simulated using vortex filament method and the exact Biot-Savart law. Depending on the impact parameter, the rings can reconnect to produce one larger and one smaller rings or to merge into one large deformed loop. The interaction with a secondary deformed loop, created from previous ring collision, has a relatively high probability of generating small rings less than half of the size of the incoming circular ring, compared to the interaction between two circular rings.

It is also shown that the electric field has a smoothing effect on the deformed vortex rings, which explains why the vortex rings in experiments behave like perfectly circular rings even though they should be deformed after being released by the charged tangle near the tip.

Declaration

No portion of the work referred to in the thesis has been submitted in support of an application for another degree or qualification of this or any other university or other institute of learning.

Copyright Statement

(see `http://documents.manchester.ac.uk/DocuInfo.aspx?DocID=487`), in any relevant Thesis restriction declarations deposited in the University Library, The University Library's regulations (see `http://www.manchester.ac.uk/library/aboutus/regulations`) and in The University's policy on Presentation of Theses.

Acknowledgements

First of all, my sincere thanks goes to the Low Temperature Group at the University of Manchester. I would like to thank my supervisor, Prof. Andrei Golov, for his supervision and guidance throughout this course. I would also like to thank my co-supervisor, Dr. Paul Walmsley, for his patience and support. Without the help from them, this thesis would not have been possible. I thank Matthew Evans and Rory Brown for providing the initial simulation codes for this project to base on. Thanks to Alex Williams for an enjoyable time.

I am greatly indebted to my parents. They have been extremely supportive and encouraging from the very beginning. They saw the potential in me and invested in it even when I could not see it myself. Without them, I could not have made this far.

I would like to extend my appreciation to all my friends. Special thanks to Tianyue for the wonderful three years here in Manchester and for making the rainy Manchester feeling like the second place to home. Thanks to Jiajing for always being there for me.

Finally, I am grateful to everyone who has been part of my life during the past year, even though I could not mention them all in person one by one.

Chapter 1

Introduction

1.1 Superfluid Helium

A state known as a superfluid occurs in helium when it is cooled down to temperatures below the λ-point T_λ, which is approximately 2.17 K for ^{4}He. This phenomenon was first recognised in two independent papers by Kapitza [1] and Allen and Misener [2] in 1938. The phase diagram of ^{4}He is shown in Figure 1.1. A feature unique from other substances is that there is no conventional gas-liquid-solid triple point. The boiling point at 1 bar is 4.2 K. Solid ^{4}He only exists at pressures above 25 bar. Liquid helium between 0 K and T_λ is known as He II, compared to the name He I for liquid helium above T_λ.

According to the two-fluid model by London [4], Tisza [5] and Landau [6], He II is composed of two interpenetrating fluids: the normal fluid (with density ρ_N and velocity $\mathbf{v}_N$) has conventional entropy and viscosity while the superfluid (ρ_S, $\mathbf{v}_S$) possesses no entropy or viscosity. Therefore, the total density of He II is given by $\rho = \rho_S + \rho_N$ and the mass flux is $\boldsymbol{j} = \rho_N \mathbf{v}_N + \rho_S \mathbf{v}_S$. As shown in Figure 1.2, experimental evidence [7] indicates that the proportion of superfluid in He II, ρ_S/ρ, rises up with decreasing temperature and the normal component becomes almost negligible below 1 K.

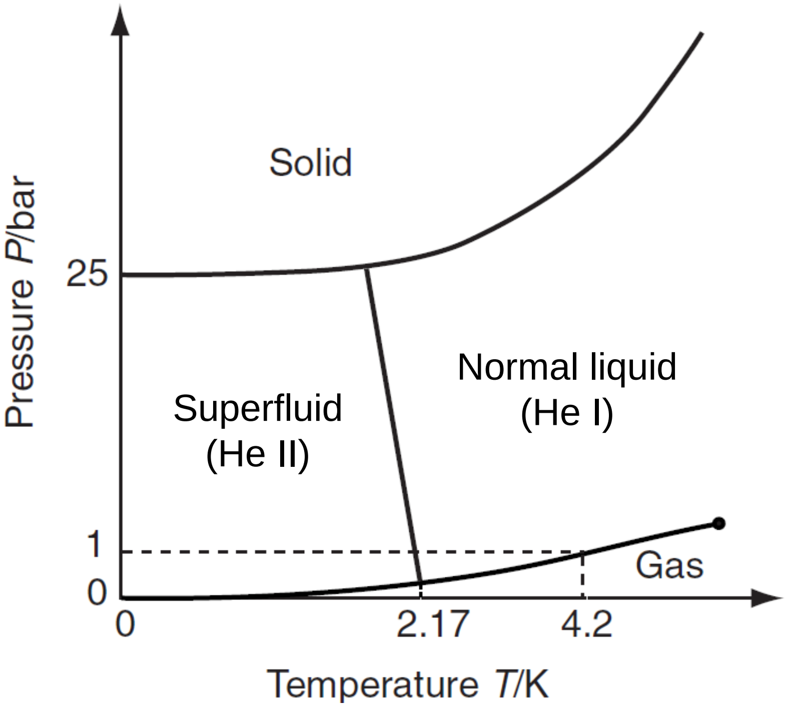

Figure 1.1: Phase diagram of ^{4}He [3].

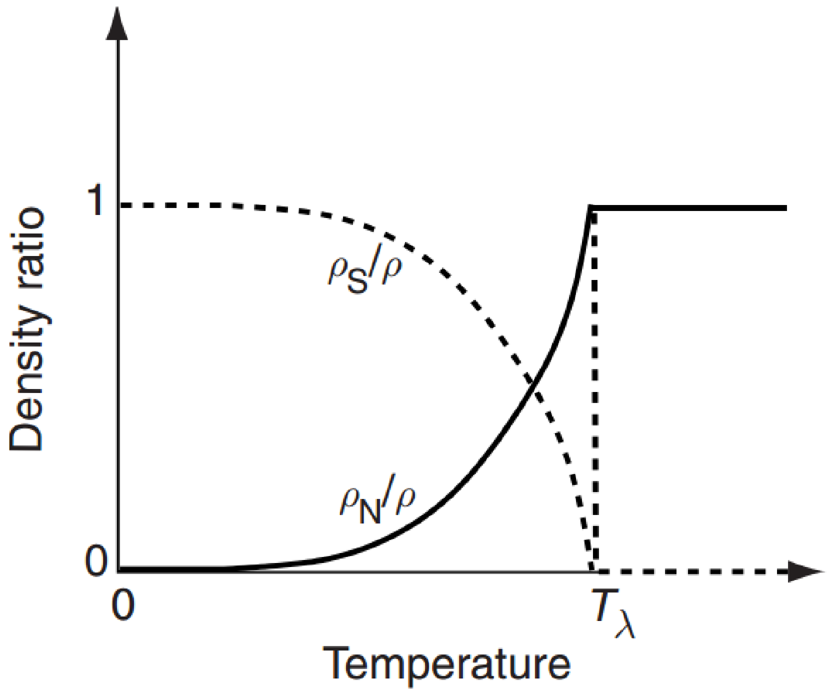

Figure 1.2: Temperature dependence of the fraction of superfluid (ρ_S/ρ) and normal fluid (ρ_N/ρ) in He II [3].

Now we look at the properties of superfluid helium microscopically. At very low temperatures, the particles tend to stay at the lowest possible energy level [3]. For a boson system such as liquid ^{4}He below the λ-point, there exists a condensate, where a single quantum state is occupied by a macroscopically large number of particles. This condensate can be described using a single coherent wave function, in the form of

$$\psi\left(\boldsymbol{r},t\right)=\psi_0\left(\boldsymbol{r},t\right)\exp\left[iS\left(\boldsymbol{r},t\right)\right], \tag{1.1}$$

where the phase $S\left(\boldsymbol{r}\right)$ is a real function of position $\boldsymbol{r}$ and time t [8]. Application of the momentum operator $\hat{\boldsymbol{p}}=-i\hbar\nabla$ to Equation 1.1 gives us the canonical momentum $\boldsymbol{p}=\hbar\nabla S$. The superfluid component moves with the velocity of the condensate, $\mathbf{v}_S$. The momentum of one constituent particle is $\boldsymbol{p}=m_4\mathbf{v}_S$, with m_4 being the mass of ^{4}He atom. Combining the above two equations , we obtain

$$\mathbf{v}_S=\frac{\hbar}{m_4}\nabla S, \tag{1.2}$$

i.e., the velocity of superfluid is proportional to the gradient of the phase. From this, we know that $\nabla\times\mathbf{v}_S=0$ and the superfluid component of He II is irrotational.

An important concept in fluid dynamics is the circulation, which is defined as the integral of the velocity around a closed path, $\oint\mathbf{v}_S\cdot\mathrm{d}\ell$. The idea of quantised circulation in superfluid helium was first raised by Onsager [9]. If $\psi\left(\boldsymbol{r},t\right)$ in Equation 1.1 is to have a physical meaning, it must be single-valued and thus the phase change around a loop must be an integral multiple of 2π or zero. We have

$$\oint\mathbf{v}_S\cdot\mathrm{d}\ell=2\pi n\frac{\hbar}{m_4}=n\frac{h}{m_4}, \tag{1.3}$$

where $n=0,1,2,\ldots$. The circulation is quantised in units of $\kappa=h/m_4\approx$ $9.98\times10^{-4}\,\mathrm{cm}^2\,\mathrm{s}^{-1}$.

The first experiment to detect the quantum of circulation in He II was carried out by Vinen [10] in 1961, using a fine wire stretched along the centre of a cylindrical vessel containing He II. A circulation of superfluid was established by rotating the whole apparatus uniformly about the axis of both the wire and the cylinder. The measurement was achieved owing to the Magnus effect on the modes of transverse vibrations of the wire. The results have showed that the quantised circulation is in units of h/m.

This thesis is concerned with the dynamics of vortex rings in superfluid helium and how they interact with each other. The plan for this thesis follows. The rest of this chapter introduces the basic concepts and relevant research work. Chapter 2 contains the analysis of the on-going experiments performed at Manchester on charged vortex rings in ^{4}He. Chapter 3 is for the simulations on the collisions of two vortex rings initially travelling in the same direction. Chapter 4 is devoted to the dynamics of a singly-charged vortex ring in an electric field. Chapter 5 discusses the results and makes conclusions.

1.2 Vortex Ring

The topic of vortex rings has a long and rich history. In classical fluid mechanics, Saffman and Baker [11] defined a *vortex* as a finite volume of rotational fluid bounded by irrotational fluid or solid walls. A *vortex line* is a curve tangent to its vorticity $\boldsymbol{\omega} = \nabla \times \boldsymbol{v}$. A *vortex tube* is a cylinder of small to infinitesimal cross section whose surface comprises of vortex lines. A vortex tube surrounded by irrotational fluid makes a *vortex filament*. In 1955, Feynmann [12] suggested that the vortices in superfluid might take the form of a vortex filament with a hollow core of atomic dimensions.

Considering a single straight vortex line among the vortices in He II at absolute

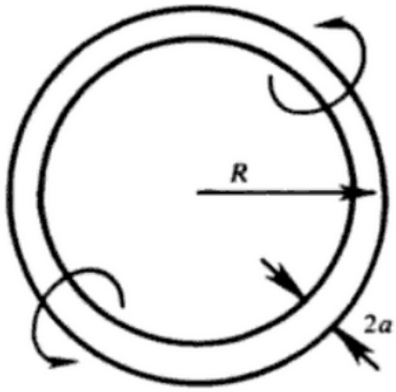

Figure 1.3: A vortex ring with radius R and core radius a [13].

zero, i.e., pure superfluid helium, if we take the contour of radius r, we have

$$\kappa = \oint \mathbf{v}_S \cdot \mathrm{d}\ell = 2\pi r \mathbf{v}_S(r) = n\frac{h}{m_4}, \tag{1.4}$$

which gives

$$\mathbf{v}_S(r) = \frac{\kappa}{2\pi r}. \tag{1.5}$$

The velocity is proportional to the inverse of radius r. For a vortex line with core radius a, the kinetic energy per unit length is

$$K = \int_a^b \frac{1}{2}\rho_S \mathbf{v}_S^2 \mathrm{d}r^2 = \frac{\rho_S \kappa^2}{4\pi} \ln(b/a), \tag{1.6}$$

where b is of the order of the mean distance between vortices.

Another simple vortex structure is a circular vortex ring, which could be seen roughly as a vortex line with its head connected to its tail. A schematic plot of a vortex ring with radius R and core radius a is presented in Figure 1.3. Roberts and Donnelley [14] proved that vortex rings could be described by a total energy E equivalent to a Hamiltonian such that their velocity and impulse satisfy the Hamilton's equation $v = \partial E/\partial P$. When the core radius a of a thin vortex ring is negligible compared to the ring radius R, the energy is

$$E = \frac{1}{2}\rho\kappa^2 R \left[\ln\left(\frac{8R}{a}\right) - \alpha\right]. \tag{1.7}$$

The impulse is expressed as

$$P = \rho\kappa\pi R^2. \tag{1.8}$$

The vortex ring moves forward with its self-induced velocity

$$\begin{aligned} v &= \frac{\kappa}{4\pi R}\left[\ln\left(\frac{8R}{a}\right) - \beta\right] \\ &= \frac{\partial E}{\partial P} = \frac{\kappa}{4\pi R}\left[\ln\left(\frac{8R}{a}\right) + 1 - \alpha\right]. \end{aligned} \tag{1.9}$$

For classical vortex ring with hollow core at constant pressure, the parameters are $\alpha = 3/2$ and $\beta = \alpha - 1 = 1/2$.

One of our research interests is the behaviour of a charged vortex ring inside an electric field in superfluid helium. The force on a ring moving in electric field E with N particles of charge e trapped on it could be written as

$$F = eNE = \frac{\mathrm{d}P}{\mathrm{d}t} = 2\pi\rho\kappa R\frac{\mathrm{d}R}{\mathrm{d}t}. \tag{1.10}$$

Quantised vortex rings were first studied by Rayfield and Reif [46] in 1964, using an ion time-of-flight spectrometer. Accelerated ions from a radioactive cathode could lead to charged vortex rings in He II. The behaviours of the charge carriers were tested at 0.3 K with little dissipation and the theoretical calculations were based on a solid core vortex model with slightly different α and β. It was shown that the charge carriers behave exactly like vortex rings with circulation $\kappa = h/m_4$ and the expressions for energy, impulse and velocity in an inviscid fluid were verified.

1.3 Quantum Turbulence

In the study of the flow of classical fluids, turbulence, as a complex non-linear phenomenon, is involved in fields ranging from engineering to meteorology to astrophysics, and thus understanding turbulent behaviours is of great importance to us. It is possible to describe turbulence of an incompressible fluid via the Navier-Stokes equation [16]:

$$\partial_t \boldsymbol{v} + \boldsymbol{v} \cdot \nabla \boldsymbol{v} = -\nabla p + \nu \nabla^2 \boldsymbol{v}, \tag{1.11}$$

$$\nabla \cdot \boldsymbol{v} = 0, \tag{1.12}$$

where $\boldsymbol{v}$ is the velocity, p is the pressure and ν is the kinematic viscosity.

A dimensionless control parameter of the flow, the Reynolds number, is defined as, [17]

$$R = \frac{LV}{\nu}, \tag{1.13}$$

with L being a characteristic scale, V the velocity of the flow and ν the viscosity. High Reynolds number describes turbulent flows and low Reynolds number is associated with smooth laminar flows.

Although classical turbulence has been studied and modeled by scientists since the time of Leonardo da Vinci, a relatively young research field called quantum turbulence has only been brought to our attention in the last century. Quantum fluids, such as superfluid, exhibit quantum turbulence phenomenon. Feynman [12] first raised the theoretical possibility of turbulence in superfluid due to the quantised vortex lines in 1955. Later, Hall and Vinen [18] found experimental evidence of turbulent characteristics in rotating He II. The theoretical and experimental discoveries of mutual friction [18,19], which arises from the scattering of thermal excitations in the normal component of the superfluid by the vortex lines, contribute to our knowledge of quantum turbulence.

The decay of the quantum turbulence in the zero temperature limit has become an important topic in recent years. Walmsley and his coworkers in Manchester [20, 21] used negative ions in the form of electron bubbles to probe the decay of turbulence in superfluid ^{4}He between 0.08 K and 1.6 K. A vortex tangle was produced by an impulsive spin-down of the cubic experiment cell from rotational equilibrium to rest. Pulses of electrons were injected by tungsten field-emission tips. The dominant charge carrier changes from free ions at temperatures higher than 0.8 K to trapped electron bubble inside the core of vortex rings below 0.7 K. They discovered two types of late-time decays of the density of quantised vortex lines.

1.4 Vortex Filament Method

In the pioneering work by Schwarz [22] in 1985 and 1988, the vortex filament model was developed, which treats the vortex line as an infinitely thin curve. A vortex filament is divided into small vortex segments of the form $\boldsymbol{s} = \boldsymbol{s}(\xi, t)$, where ξ is the length of each segment and t is the time. In the zero temperature limit, dissipation is absent and only the Magnus force acts on the vortices. Each segment moves with the velocity of the superfluid component $\mathbf{v}_S$ given by Biot-Savart law:

$$\mathbf{v}_S(\boldsymbol{s}, t) = \frac{\kappa}{4\pi} \int \frac{(\boldsymbol{s}_1 - \boldsymbol{s}) \times \mathrm{d}\boldsymbol{s}_1}{|\boldsymbol{s}_1 - \boldsymbol{s}|^3}. \tag{1.14}$$

Here $\boldsymbol{s}_1$ refers to a particular point on the curve. The line integral is along all the vortices. It has a singularity at $\boldsymbol{s}$, which could be solved if the finite vortex core size a is taken into account:

$$\mathbf{v}_S = \frac{\kappa}{4\pi} \hat{\boldsymbol{s}}' \times \boldsymbol{s}'' \ln\left(\frac{2\sqrt{\ell_+ \ell_-}}{e^{1/2} a}\right) + \frac{\kappa}{4\pi} \int' \frac{(\boldsymbol{s}_1 - \boldsymbol{s}) \times \boldsymbol{s}_1}{|\boldsymbol{s}_1 - \boldsymbol{s}|^3}, \tag{1.15}$$

where $\hat{\boldsymbol{s}}'$ and $\boldsymbol{s}''$ are the unit tangent and normal vectors at $\boldsymbol{s}$ respectively. ℓ_+ and ℓ_- refer to the lengths of the two vortex segments connecting at point $\boldsymbol{s}$ and the integral is over the other segments that are not connected to $\boldsymbol{s}$. The first term on the right hand side is called the local term and the second term is for the non-local contribution.

In the local induction approximation (LIA) [23, 24], only the local term is retained. This is more convenient both analytically and computationally compared to the Biot-Savart approach, as the growth in the cost of the computation is proportional to N under LIA while the inclusion of the non-local term raises the constant of proportionality to N^2. However, the use of LIA is limited. It is sufficient to describe turbulence where the long-range effects cancel out. For turbulence under rotation or strongly perturbed vortex filaments, the non-local term is essential. One such example is that LIA generates unreliable results in the evolution of vortex knots [25].

1.5 Relevant Research

NLSE model

Another common model for quantised vortex rings is the non-linear Schrödinger equation (NLSE), also known as the Gross-Pitaevski (GP) equation. NLSE works accurately for a system of weakly interacting bosons but can only be seen as a qualitative model for superfluid helium due to stronger interactions. For Bose particles with mass m, we have [26, 27]

$$i\hbar\frac{\partial\Psi}{\partial t} = \left(-\frac{\hbar^2}{2m}\nabla^2 + V_0|\Psi|^2 - E\right)\Psi, \tag{1.16}$$

where Ψ is the condensate wave function, V_0 describes the boson-boson repulsion and E is the increase in energy when one boson is added. Compared to the vortex filament method in the previous section, NLSE describes the quantum effects on very small lengths scales with high resolution, which in turn limits its performance on calculations involving large vortex rings. NLSE applies only to superfluid at absolute zero while the mutual friction term could be easily taken into account in the vortex filament model.

Vortex reconnection

One unique feature of quantum turbulence is the vortex reconnection, occurring upon close approach of vortices. Schwarz [22] gave explicit descriptions of a few different reconnection scenarios using an added algorithm in the vortex filament method. It was later demonstrated using NLSE, where the reconnections would occur naturally, by Koplik and Levine [28] in 1993, when they studied the reconnections of vortex lines of different initial orientations.

Dissipation mechanisms at $T = 0$

The cascade of the Kelvin waves, i.e., the helical waves on vortex filaments, serves as one of the dissipation mechanisms in the zero temperature limit that transfers energy to higher and higher wave numbers. Kerr [29] showed that a cascade could be initiated by vortex stretching of a pair of perturbed antiparallel quantum vortices using the GP equations, which lead to the generation of a series of vortex rings. Kursa *et al.* [30] demonstrated a cascade of vortex rings initiated by the reconnection of two nearly antiparallel vortex lines, which should be an efficient decay mechanism for less dense tangles at very low temperatures. By the application of a driving force to a rectilinear vortex between two parallel sheets with periodic boundaries, Vinen *et al.* [31] confirmed the development of a steady state cascade, which was remarkably insensitive to strength and frequency of the drive.

Two competing theories were proposed by L'vov and Nazarenko [32] and by Kozik and Svistunov [33], regarding the approaches for the Kelvin wave cascade. Baggaley and Laurie [34] modeled a single periodic vortex line forced from rest and obtained data in agreement with the theory by L'vov and Nazarenko [32]. In 2011, Baggaley and Barenghi [35] analysed a few different configurations of vortex filaments and investigated the conditions for a Kelvin wave cascade in superfluid helium. No Kelvin wave cascade was observed for a single perturbed vortex line, a perturbed vortex ring or two circular vortex rings linked together, but three parallel perturbed vortex lines, three perturbed rings in the same direction and two linked perturbed rings could all induce the cascades. The simulations showed that the Kelvin wave cascade could be initiated not only by the reconnections but also by the interactions of nearby vortices via the velocity field.

Vortex ring interactions

Understanding the interactions between a pair of vortex rings can shed light on the microscopic processes in quantum turbulence. In 1996, Koplik and Levine [36] considered the symmetric annihilation in a head-on collision and the semisymmetric scattering of two identical vortex rings for the generation of vorticity in superfluids. Leadbeater *et al.* [37] collided two vortex rings of the same size with axes offset by a distance and showed that reconnections could result in the radiation of energy through sound pulses. The reconnections of vortex rings in three different configurations (in offset collision, with different radii and linked at 90°) with small Reynolds number were investigated by Chatelain *et al.* [38] by solving the Navier-Stokes equations and an intensification of dissipation was observed. Caplan *et al.* [39] studied the scattering of two unit circulation vortex rings, but unlike aforementioned work by Koplik and Levine [36], they focused on the co-planar offset collisions. For rings with opposite circulation, depending on the offset, the two rings could annihilate, miss each other, or merge and then split into two new perturbed rings travelling away from each other at a scattering angle, which was a function of initial radii and impact parameter. In addition, they proposed effective equations of motion for a pair of co-axial vortex rings of the same circulation, which produced good agreement when tested against the original NLSE model for leapfrogging evolution. In the case of reconnecting two linked planar vortex rings at finite temperatures done by Hänninen [40], it was found that Kelvin waves induced by the reconnection could increase energy dissipation greatly but not angular momentum. In contrast to what Kivotides *et al.* have discovered [41], no Kelvin wave cascade was observed to be triggered by a single reconnection event; rather the energy was dissipated through mutual friction damping.

Although numerous simulations have been performed using vortex rings, the case where two rings are initially travelling in the same direction has not attracted much attention. In 2003, Leadbeater *et al.* [42] considered the situation where a large ring and a small ring both propagated in $+x$ direction with their axes offset by a certain amount and then collided, leading to the disappearance of the small ring. As Kelvin waves were excited on the merged vortex ring due to the reconnections, they examined the loss of line length during the process and found a constant Kelvin-wave decay coefficient, which was consistent with established experimental results. One well-studied case in this setup is when two rings are coaxial, which results in the leapfrogging motion, as confirmed by Caplan *et al.* [39] and Wacks *et al.* [43]. In a study of the inverse energy transfer induced vortex reconnections, Baggaley *et al.* [44] injected a large number of rings of random radius travelling in the same direction into a periodic box. They discussed the outcomes of the two types of collisions between the rings: the radii of the rings roughly remained the same after head-on collisions, while the collisions from behind created rings with considerably different sizes. The interactions between two vortex rings travelling in the same direction with certain axial offset are investigated in detail in Chapter 3, in attempt to fill the void in this research area.

Chapter 2

Experimental Analysis

This chapter includes an analysis for the experimental data from the ongoing experiment at the University of Manchester. The experiment is set up as stated in Section 2.1. In Section 2.2, we provide a comprehensive analytical calculation for the dynamics of a charged vortex ring (CVR) inside the experimental cell. The experimental analysis is divided into two main sections according to the aims of the experiments: Section 2.3 discusses the voltage dependence while Section 2.4 considers the temperature dependence.

2.1 Experiment Setup

The setup is shown in Figure 2.1, which is a modified version of an earlier experiment [45]. The experimental cell is filled with liquid ^{4}He at temperature below 0.8 K. The cell is divided into two compartments by a mid-plate of negligible thickness. The height of the first part is $d_1 = 15$ mm. A drive voltage, V_{drive}, is applied across this region to impose an electric field. The mid-plate has a hole in the centre with a diameter of 5 mm, which allows vortex rings to come through. The second section is twice the size of the first one and has a height of $d_2 = 30$ mm. The electric field in this

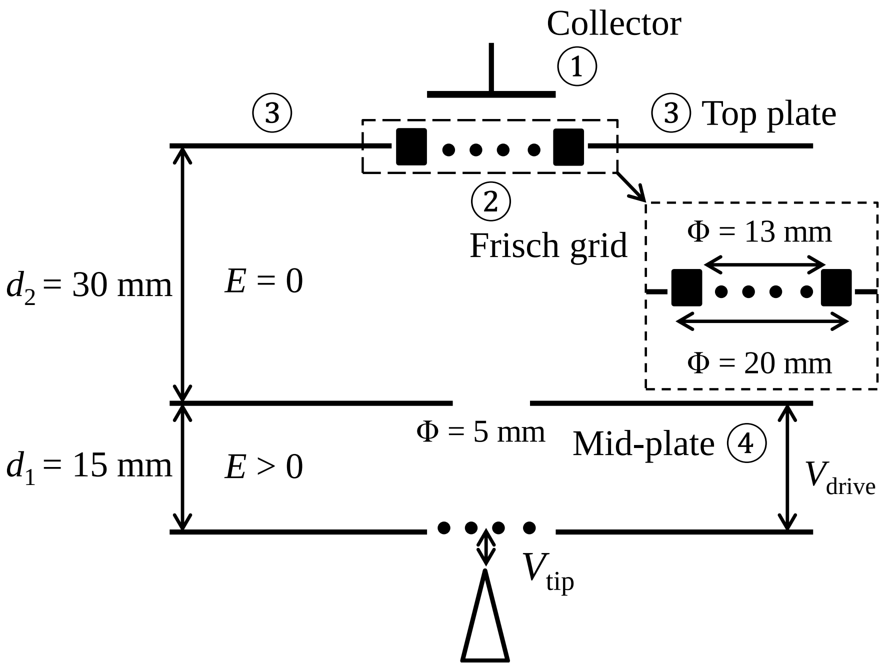

Figure 2.1: The experiment setup. The cell is divided into two sections by a mid-plate of negligible thickness, which has a hole in the centre with a diameter of 5 mm. Drive voltage is applied in the 15 mm space between the bottom plate and the mid-plate. There is no electric field in the 30 mm region between the mid-plate and the top-plate. A collector is located behind the Frisch grid in the middle of the top plate. The Frisch grid has a mesh of $\Phi = 13$ mm, which is bounded on a metal ring with a diameter of 20 mm. Current measurements are made at the 4 locations inside the cell labelled in the graph.

section is kept at zero. A Frisch grid with a mesh, which has a geometric transparency of 92%, is embedded in the middle of the top plate. The mesh has a diameter of 13 mm and is bounded on a metal ring with a diameter of 20 mm, as shown in the enlarged dashed panel. A collector is hidden behind this grid and is shielded from displacement current. The currents received by the collector, the Frisch grid, the top plate and the mid-plate are simultaneously monitored and analysed. The time constant of the detection electronics is approximately 0.1 s.

Pulses of CVRs are fired from a tungsten tip into the cell. Tip voltage, V_{tip}, refers to the voltage between the tip and the bottom grid which pushes the rings into the cell. Both the tip voltage and the pulse duration are varied during the experiment.

The CVRs are actually injected in a broad range of angles. Although the electric field imposed by the drive voltage is able to align the rings to travel almost parallel to its direction, the size of the beam is still much greater than the 5 mm diameter of the hole in the mid-plate. Consequently, most of the CVRs hit the plate and only a few percent are able to travel through. We assume that the hole poses no effect on the velocity or the direction of the rings that are moving through. The remaining rings now enter the field-free region and proceed until they hit the top plate, the Frisch grid or the collector. The drive voltage is switched between certain values for each tip voltage applied.

The motivation to modify the cell upon previous design is to observe CVRs and their interactions in the field-free region. It also serves to investigate the release of the CVRs from the localised compact charged tangle that builds up near the tip, which is realised by the insertion of the mid-plate.

2.2 Time of Flight Calculation

The experimental results are compared against the results of theoretical calculations. The equations for the energy and the velocity of a CVR of radius R carrying one elementary charge e at absolute zero are discussed in Chapter 1 and can be found in Equations 1.7 and 1.9. The density of superfluid helium is $\rho = 0.145\,\mathrm{g\,cm^{-3}}$ and $\kappa = 9.98 \times 10^{-4}\,\mathrm{cm^2\,s^{-1}}$ is the quantum of circulation. Since the logarithm term $\ln\left(\frac{8R}{a}\right)$ does not vary much with the change in radius R in our analytical calculation, it is treated as a constant and is given the Greek symbol Λ. The specific value of Λ is discussed in each section below.

The calculation of the time of flight for a CVR to reach the collector at zero temperature limit can be split into two parts. In the first part, we consider the time for the ring to travel across the electric field and arrive at the mid-plate. For a singly-charged vortex ring with initial radius R_0, its energy is proportional to its radius R and the change in the energy equals to the energy gained or lost by the charge in the electric field at position x, i.e.,

$$\Delta E = \frac{1}{2}\rho\kappa^2 \left(R - R_0\right)\left(\Lambda - \frac{3}{2}\right) = \frac{eV_{drive}}{d_1}x. \tag{2.1}$$

The radius of the ring at the mid-plate, in other words, at position $x = d_1 = 15\,\text{mm}$, is

$$R_1 = \frac{2eV_{drive}}{\rho\kappa^2\left(\Lambda - 3/2\right)} + R_0. \tag{2.2}$$

The velocity of the CVR is derived by substituting the ring radius at this point into Equation 1.9:

$$v_1 = \frac{\kappa}{4\pi R_1}\left(\Lambda - \frac{1}{2}\right). \tag{2.3}$$

The time of flight to the mid-plate is

$$\begin{aligned} t_1 &= \int_0^{d_1} \frac{\mathrm{d}x'}{v} = \int_0^{d_1} \frac{4\pi R_1}{\kappa\left(\Lambda - \frac{1}{2}\right)}\mathrm{d}x' \\ &= \frac{2\pi\left(R_1 + R_0\right)}{\kappa\left(\Lambda - 1/2\right)}d_1. \end{aligned} \tag{2.4}$$

If the CVR has successfully passed through the hole in the mid-plate, assuming that there are no interactions with other CVRs, it travels at constant velocity v_1 in the absence of electric field until it reaches the top of the cell. The ring radius remains unchanged. The time of flight in this field-free region is

$$t_2 = \frac{d_2}{v_1} = \frac{4\pi R_1 d_2}{\kappa\left(\Lambda - 1/2\right)}, \tag{2.5}$$

with $d_2 = 30$ mm. Combining the time of flight in these two separate regions gives us the total time of flight in the cell,

$$\begin{aligned} t &= t_1 + t_2 \\ &= \frac{2\pi\left(R_1 d_1 + R_0 d_1 + 2R_1 d_2\right)}{\kappa\left(\Lambda - 1/2\right)}. \end{aligned} \tag{2.6}$$

The above calculations are based on the approximation that the temperature is so close to absolute zero that the mutual friction term, which arises from the interactions between the vortex lines and the thermal excitations in the normal component, could be ignored. A detailed calculation of the dynamics of a vortex ring with elementary charge e moving in a uniform electric field E at finite temperature T is given by Rayfield and Reif [46]. At T, the drag force per unit length due to mutual friction on the same CVR is $\alpha\kappa\rho v$. The dimensionless dissipative mutual friction parameter, $\alpha\left(T\right)$, is [47]

$$\alpha\left(T\right) = 25.3 \exp\left(\frac{-8.5}{T}\right) T^{-1/2} + 5.78 \times 10^{-5} T^5, \tag{2.7}$$

where T is in Kelvins. Therefore, the total force on the ring is

$$F_T = eE - \frac{1}{2}\alpha\rho\kappa^2\left(\Lambda - \frac{1}{2}\right). \tag{2.8}$$

The behaviour of the CVR depends on the magnitudes of the electric field term and the mutual friction term: the CVR grows linearly with distance if the field term is larger, maintains its size if the two terms are equal or shrinks if the mutual friction term is larger. The change in ring energy corresponds to the work done by the total force, which writes

$$\Delta E' = \frac{1}{2}\rho\kappa^2\left(R - R_0\right)\left(\Lambda - \frac{3}{2}\right) = F_T x. \tag{2.9}$$

Simplifying the above equation and substituting in $x = d_1$ give the radius at the mid-plate,

$$R_1' = \frac{2F_T d_1}{\kappa^2\rho\left(\Lambda - \frac{3}{2}\right)} + R_0. \tag{2.10}$$

The equation for time of flight is the same as Equation 2.4:

$$t_1' = \frac{2\pi\left(R_1' + R_0\right)}{\kappa\left(\Lambda - 1/2\right)} d_1. \tag{2.11}$$

As soon as the CVR enters the region with no electric field, the first term in the total force disappears and the ring starts to shrink. The new total force on the CVR is

$$F_T' = -\frac{1}{2}\alpha\rho\kappa^2\left(\Lambda - \frac{1}{2}\right). \tag{2.12}$$

Applying the same energy and work analysis used for Equation 2.9, the final radius is derived as

$$R_2' = \frac{2F_T' d_2}{\kappa^2\rho\left(\Lambda - \frac{3}{2}\right)} + R_1'. \tag{2.13}$$

Time spent in the field-free region is

$$t_2' = \frac{2\pi\left(R_1' + R_2'\right)}{\kappa\left(\Lambda - 1/2\right)} d_2. \tag{2.14}$$

Hence the total time of flight is

$$\begin{aligned} t' &= t_1' + t_2' \\ &= \frac{2\pi}{\kappa\left(\Lambda - 1/2\right)}\left(R_0 d_1 + R_1' d_1 + R_1' d_2 + R_2' d_2\right). \end{aligned} \tag{2.15}$$

2.3 Voltage Dependence

Charged vortex rings are injected into the cell with a pulse length of 0.05 s or 0.10 s. The next pulse is injected only when most of the CVRs in the current pulse have arrived at the top plate after typically 200 - 300 s, allowing any turbulence to dissipate. Three tip voltage values, 400 V, 350 V and 300 V, were selected for the 0.05 s case and more values, 400 V, 375 V, 350 V, 330 V, 310 V, 290 V and 270 V, were used in the 0.10 s case. For each tip voltage, the drive voltage was varied for 23 different values between 2 V and 200 V. The experimental temperature was set to approximately 0.1 K with small fluctuations, at which the effects of the mutual friction can be ignored. These small differences in temperature did not show any impact on our results, as the data remains consistent with reasonable errors.

Figure 2.2 offers an overview of the currents received at the four channels inside the cell for six selected drive voltages. The time $t = 0$ corresponds to the middle of the injection pulse. The tip voltage is kept at 400 V. The currents for CVRs injected with a pulse length of 0.05 s are plotted in solid curves and compared to the dashed curves for the 0.10 s pulse length. A clear increase in currents on every channel is observed due to the longer pulse length, but it is not in proportion to the doubling in pulse length. The widths of the current peaks, t_{width}, which are defined as the full width at half maximum (FWHM) of the time, vary as the drive voltage increases. The currents start to rise earliest for the mid-plate and latest for the collector, indicating the time of first occurrence of the CVRs at locations inside the cell. The peak position of the mid-plate current stays at around 0.25 s regardless of the increasing drive voltage, while the peaks of the currents on the other three channels shift considerably from about 0.5 s to 1.3 s, of which the indications will be explained in the following paragraphs.

The current data from each channel was processed. Useful numbers, including peak time, t_{peak}, peak current, I_{peak}, time at the edge of the peak where current starts to rise, t_{edge}, and the width of the peak, t_{width}, were extracted. Calculations were performed to provide the total charge received, Q_{total}, the percentage of the rings through the mid-plate, r_{through}, the ratio of the spread on the top plate, r_{spread}, as well as the effective transparency of the Frisch grid, T_{g}. The analytical time of flight in the two regions of the experimental cell was computed according to the equations listed in Section 2.2. The analysis for the mid-plate data and the collector data is among our primary points of concern. Since the two sets of data acquired for different pulse lengths mostly

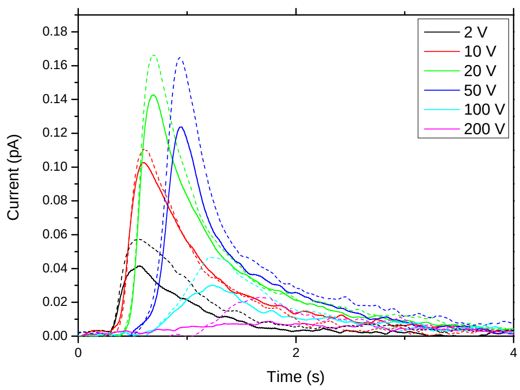

(a) Channel 1 (collector)

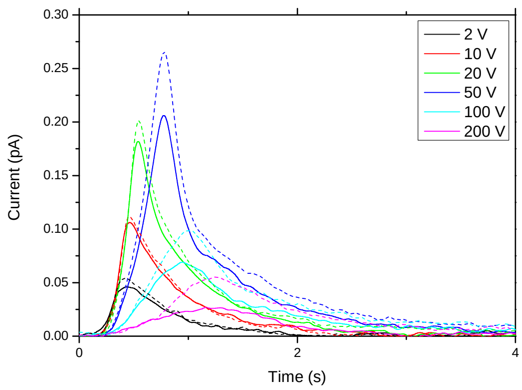

(b) Channel 2 (Frisch grid)

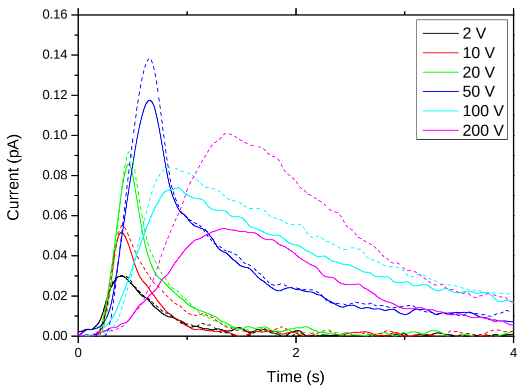

(c) Channel 3 (top plate)

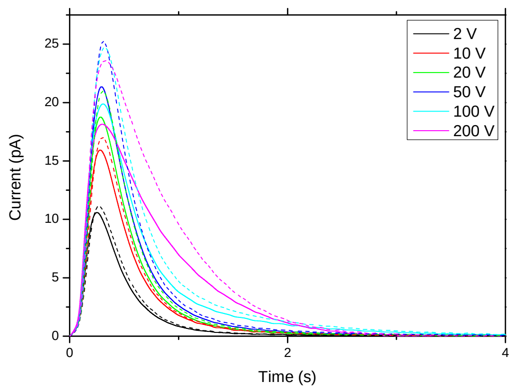

(d) Channel 4 (mid-plate)

Figure 2.2: Currents received at four different locations inside the cell at the same tip voltage of 400 V for six selected drive voltages specified in the legend. Position of each channel is as labeled in Figure 2.1. $t = 0$ corresponds to the middle of the injection pulse. The solid curves represent the case with 0.05 s pulse length and the dashed curves are for the pulse length of 0.10 s.

resemble each other, we focus on the 0.05 s case for most of the demonstration and only discuss the 0.10 s case when major differences occur.

The injection tip generates a dense tangle of charged vortices, which is pulled towards the injector grid by the electric field created from the tip voltage. Figure 2.3 (a) helps to demonstrate what is happening between the tip and the injector grid. CVRs are released from the dense tangle and travel in different directions, which should then be aligned by the electric field. Although a rectangular pulse of charge is injected, the injection of the CVRs into the cell is actually according to a distribution similar to what

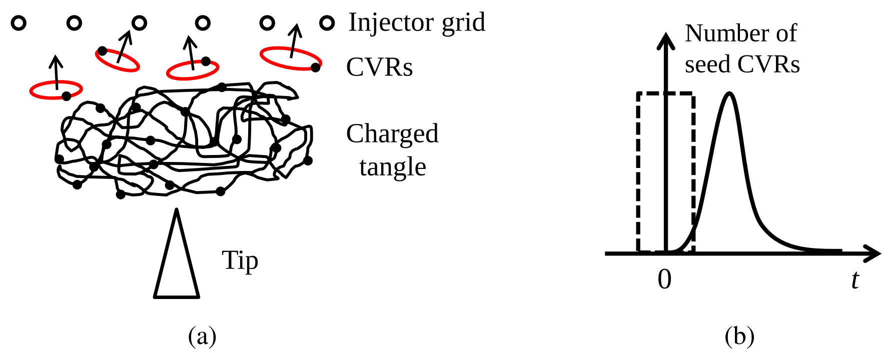

Figure 2.3: (a) The release of CVRs from the dense charged vortex tangle near the tip. The released CVRs are pushed by the tip voltage to travel through the injector grid into the experimental cell. The solid black dots represent the electric charges and most CVRs carry one elementary charge. (b) Distribution of the number of seed CVRs injected into the experiment with respect to time. Plotted in dashed line is the rectangular pulse of tip voltage, during which electrons are injected from the tip.

is shown in Figure 2.3 (b). The signal received on the mid-plate is representative of the time scales and distribution for the release of the seed CVRs from this tangle near the tip. Time at the edge of the peak reflects the time of the CVRs first entering the cell, since displacement current is produced on the plate when the CVRs pass through the injector grid. According to Figure 2.4, t_{edge} decreases to a very small degree with the increasing drive voltage, roughly from 0.09 s to 0.07 s, suggesting that the drive voltage has helped to pull the CVRs into the cell. t_{peak} tells us the time when the largest number of CVRs are being released from the tip tangle and entering the cell, which stays at about 0.25 s for the whole range of drive voltages. This invariance indicates that the release of the CVRs from the tangle only weakly depends on the drive voltage and the tip voltage.

The collector is shielded from the displacement current by hiding behind the Frisch grid, but the top plate is still sensitive. Time at the edge of the peak for the top plate currents points out the time when first group of vortex rings has travelled past the mid-plate and entered the second section of the cell, because the charge on the CVRs will

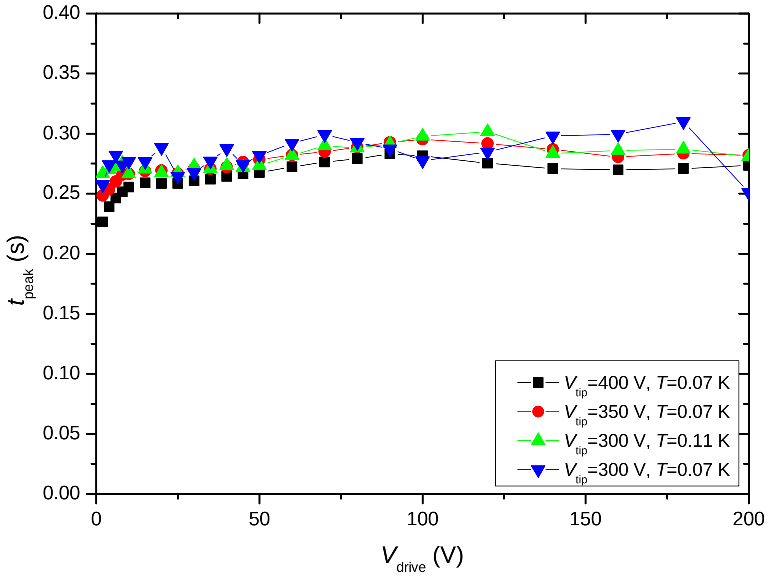

(a) Peak time

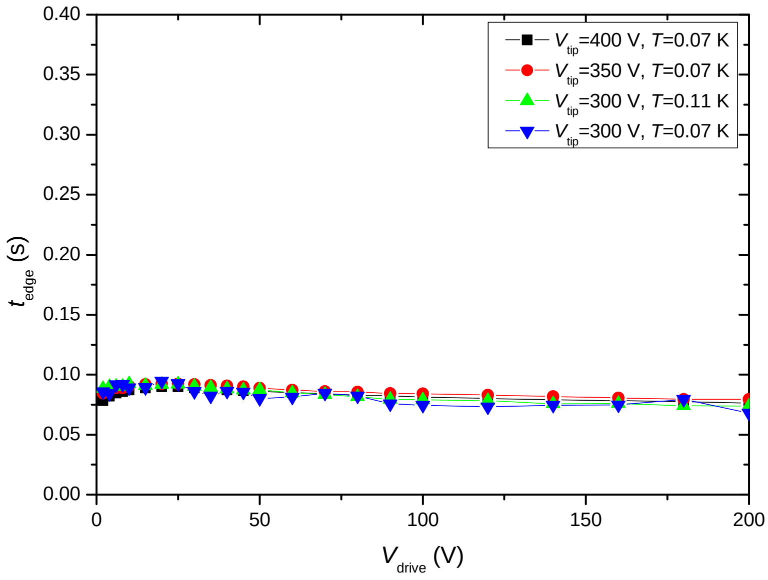

(b) Time at edge

Figure 2.4: (a) Peak time and (b) time at the edge of the peak derived from the currents received by the mid-plate, for pulse length of 0.05 s. Three tip voltage values, 300 V, 350 V and 400 V, were applied. The average temperature during the measurement was indicated in the legend and we have two sets of data for tip voltage 300 V with slightly different temperatures.

induce current on the top plate. If we ignore the thickness of the mid-plate, this t_{edge} can be regarded as the experimental time of flight to the mid-plate. The analytical calculation for a CVR to cross the electric field and reach the mid-plate was repeated for initial radii of 0.5 μm, 1.0 μm and 1.5 μm, using Equation 2.4. Altering the logarithm term Λ in the equations results in the change of the line slope. For the best fit to the experiment data, it was set to be a constant 12, which corresponds to a constant radius of $\simeq 2.6\,\mu$m. The drive voltage was varied from 2 V to 200 V to match the experiment.

The experimental time at the edge for the top plate is given in Figure 2.5, together with the analytical time of flight to the mid-plate. t_{edge} increases as the drive voltage goes up and generally agrees with the analytical results, especially at low drive voltages. The best fit for the experimental data is the analytical calculation with initial radius of 1.0 μm. It can be deduced that the charged tangle near the tip tends to release CVRs with initial radius close to 1.0 μm. This can be checked against the prediction of Kozik and Svistunov [33] that the emitted ring radius $r_* \sim \ell/[\ln \ell/a]^{1/2}$, where ℓ is the inter-vortex separation. Assuming that all power generated by the tip goes into the energy of the vortex tangle, for tip current $I \sim 300\,pA$, tip voltage $U \sim 500\,V$ and typical distance between the tip and grid $d_{tg} \sim 1$ mm, we have $\ell \sim 3\,\mu$m and thus $r_* \sim 1\,\mu$m, agreeing with our conclusion above. At low drive voltages when the precision of the data is still high, t_{edge} has a value of about 0.2 s, which suggests that it takes that amount of time for the fastest rings to pass through the mid-plate. The deviation of the experimental curves from the analytical data at higher drive voltage probably indicates the occurrence of the vortex ring interactions even before the mid-plate.

Apart from the mid-plate, the currents received by the collector are also of great interest. Since the collector is not affected by the displacement current, the peak time indicates the time that is most probable for CVRs to arrive and the time at the edge should provide the time of arrival for the fastest rings. Both of them are plotted in Figure 2.6, along with the analytical time to reach to the collector for the same three

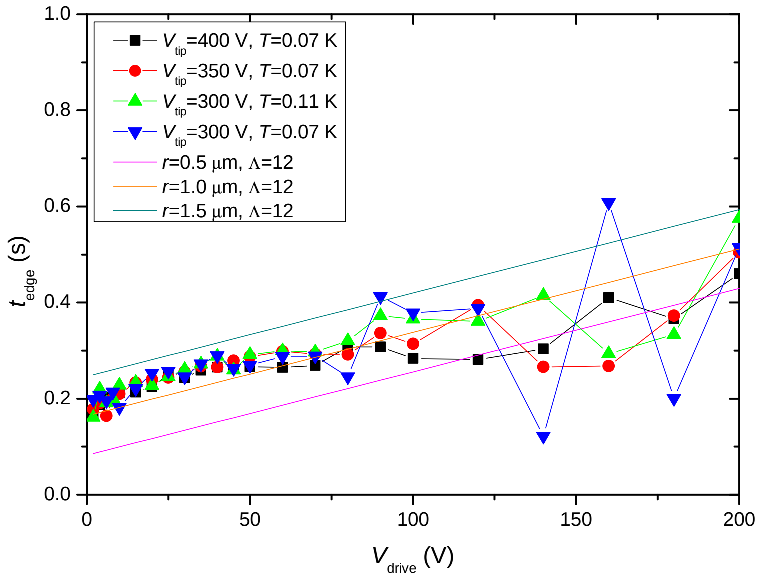

Figure 2.5: Time at the edge of the peak for currents on the top plate, for pulse length of 0.05 s. The analytical time of flight for a CVR to reach the mid-plate is provided for comparison, with Λ in equations set to 12. The three straight lines each represent a CVR of a different initial radius (0.5 μm, 1.0 μm and 1.5 μm) to reach the mid-plate at drive voltages from 2 V to 200 V, calculated using Equation 2.4.

initial radii as before. The gradient of the experimental data generally agrees with the slope of the analytical calculation, particularly at drive voltage below 100 V. The line for initial radius of 1.0 μm is the closest match to t_{peak} and it can be inferred that the injected CVRs are most likely to have an initial radius of 1.0 μm. t_{edge} is closest to the calculation for radius of 0.5 μm, which suggests that the first rings to arrive have a initial size similar to 0.5 μm. At drive voltages higher than 100 V, the experimental time of flight has become smaller than expected due to the increasing interactions between CVRs. As observed by Walmsley *et al.* [48], for a fixed tip voltage, the seed CVRs reconnect more frequent and generate more secondary vortex loops at higher drive voltage. The small secondary rings created travel faster and arrive at the collector early, leading to a much earlier rise in the time of the edge.

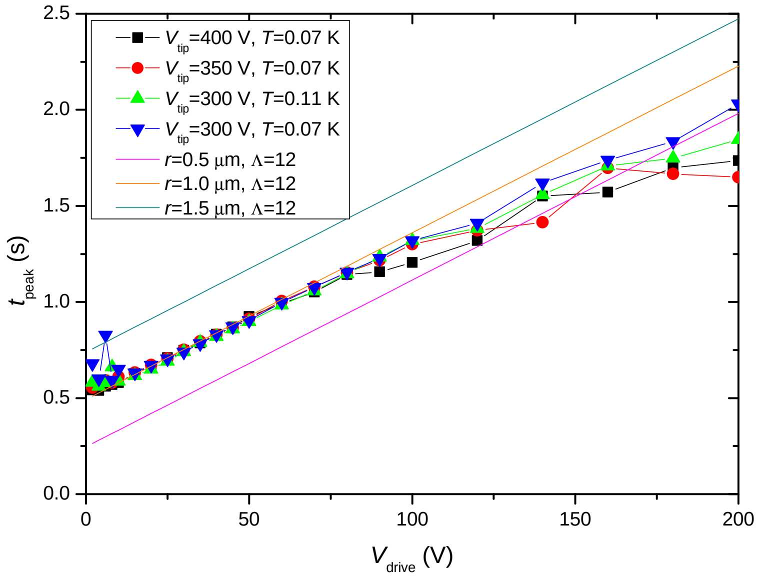

(a) Peak time

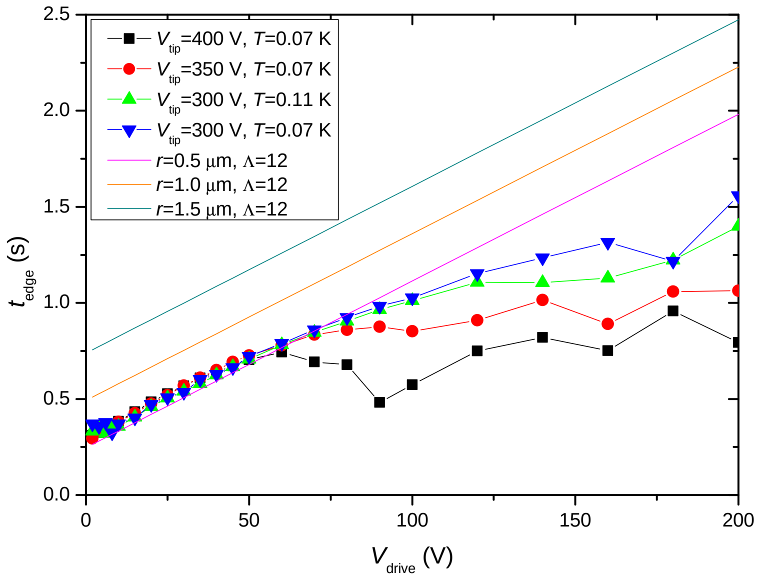

(b) Time at edge

Figure 2.6: (a) Peak time and (b) time at the edge of the peak derived from the currents received by the collector, for pulse length of 0.05 s. The three straight lines in each graph are the analytical time of flight for a ring with initial radius of 0.5 μm, 1.0 μm and 1.5 μm respectively to reach the collector at different drive voltages, according to Equation 2.6.

The early arrival of the smaller rings can be explained more explicitly by the schematic plots given in Figure 2.7. Here, the sizes of the rings are enlarged for demonstration purposes and are not in real proportion to the experimental cell. Ideally, when a CVR passes through the hole in the mid-plate, it continues its journey towards the collector with fixed velocity and radius, which is the case for majority of the rings at lower drive voltages. But since a large number of CVRs are injected into the cell together, it is likely for one CVR to reconnect with another, leaving behind at least one smaller vortex ring. The specific conditions for this kind of reconnection to happen are simulated and discussed in Chapter 3. As the velocity of a CVR is proportional to the inverse of the radius, the smaller rings travel fast and arrive at the collector early whilst the larger ones drag behind. This kind of interactions becomes more frequent at high drive voltages. It is possible for another CVR to catch up with the large secondary ring and reconnect again. Recurrence of the situation leaves us with a large charged vortex tangle, which takes a long time to finally arrive at the collector or the top plate.

Although the rings are injected with a wide range of angles, they should be quickly aligned to the direction of the drive electric field by the electric forces. The schematic plot in Figure 2.7 (b) also provides an answer to how some of the CVRs end up on the top plate rather than the collector. If two vortex rings reconnect, the magnitudes of the velocities are reassigned along with their directions. As long as the total momentum is conversed, the rings could have velocities in any directions depending on their relative positions during reconnection. Consequently, many CVRs have deviated from their original routes along the vertically upward direction and arrive at the top plate instead of the collector in the middle.

As interpreted by Golov *et al.* [49], the first component of the charge to arrive at the collector is carried by isolated CVRs, mostly the smaller rings created during reconnection. The last component to arrive is due to the slowly-moving large tangle of charged loops generated by the reconnections of the seed CVRs. These were explained

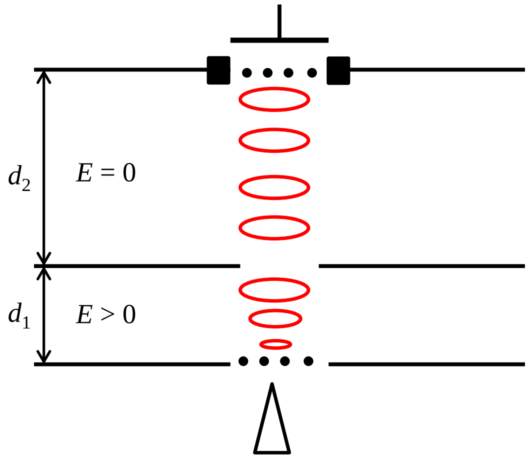

(a)

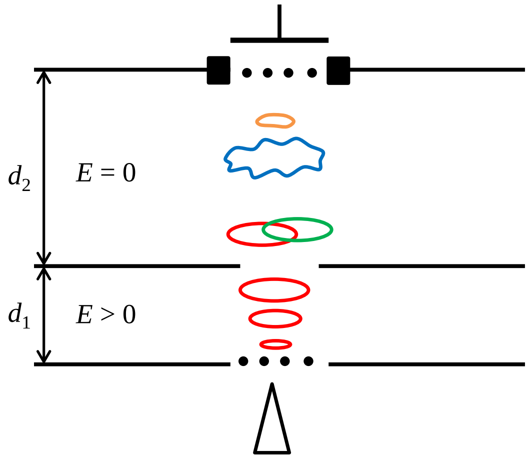

(b)

Figure 2.7: Schematic plots of the motion of a vortex ring inside the experimental cell: (a) the ring travels as an isolated ring until reaches the collector, (b) the ring reconnects with another ring and a smaller ring is generated with faster velocity, which arrives at the collector earlier than the initial ring. The sizes of the vortex rings are not in real proportion to the cell.

in detail by the schematic plots above. The width of the current peak indicates the variation in the radii of the arriving rings. From Figure 2.8, t_{width} for the mid-plate appears to be only weakly dependent on the drive voltage. It barely increases as the voltage goes up and stays at around 0.4 s for voltage below 100 V, which is reflective of the properties of the charged tangle near the tip. The tangle emits CVRs in similar sizes regardless of the drive voltage. The change in t_{width} for the collector is more obvious: it decreases with the drive voltage until reaching a minimum at about 50 V, and then starts to go up again. The decline is again explained by Golov *et al.* [49] that at small drive voltages, the currents are affected by the range of initial radii and appear to be weak and broader; while at higher voltages, the ring's radius and velocity become less sensitive to the spread of initial radius and the current peak narrows. The increase in width is probably because larger and slower tangle of CVRs is created due to the increasing number of reconnecting events. Therefore, the drive voltage of 50 V is likely to serve as the division between the dominant charge carrying mechanism: under 50 V, the charge is mostly carried by isolated CVRs, while above that voltage, the charge is carried by the vortex tangles and the CVRs produced by reconnections. It can be inferred that the distribution of the radii is narrow at 50 V.

Figure 2.9 presents the changes in the peak current on the collector and the mid-plate against the drive voltage. I_{peak} on the collector tells us the largest amount of CVRs arriving at the same time for each voltage configuration. I_{peak} on the mid-plate should represent the largest number of CVRs being released by the charged tangle near the tip at one time. For the collector data, I_{peak} reaches a maximum at around 50 V. Higher tip voltage leads to larger peak current value and lower drive voltage at the maximum. The change in the mid-plate data is more gradual and a maximum can only be noticed for higher tip voltage. The tip voltage has more influence on I_{peak} of the mid-plate than that of the collector, which again suggests that the mid-plate is sensitive to the processes occurring near the tip whilst the collector is sensitive to the processes occurring within the cloud of the emitted CVRs.

The charge accumulated on the mid-plate and the collector, obtained by integrating the current transients from 0 to 4 s, is plotted in Figure 2.10. This duration should be enough for most of the CVRs to reach any channel and be detected. The number of the CVRs that have hit the mid-plate is almost two orders of magnitude larger than that have reached the collector, because the beam of injected CVRs is much wider than

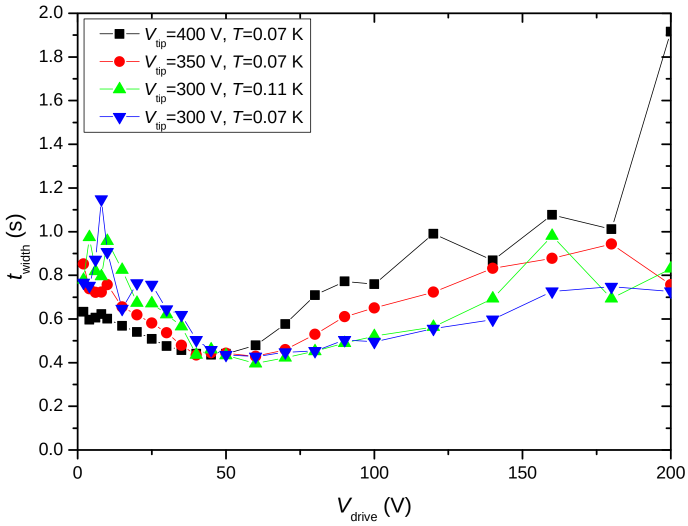

(a) Collector

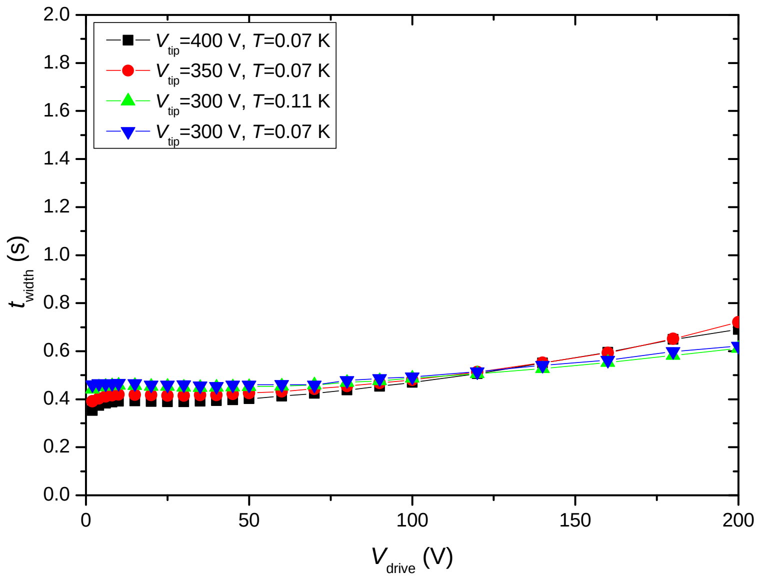

(b) Mid-plate

Figure 2.8: Width of the current peak on (a) the collector and (b) the mid-plate versus the drive voltage for pulse length of 0.05 s. It is derived by finding the time interval between the half maximum points of the peak.

the diameter of the hole in the mid-plate and majority of the rings cannot travel past. These plots reflect the trends that we observe in the peak current plots. The collector data peaks at the drive voltage of about 50 V. The mid-plate data goes up to a small degree with the increasing drive voltage.

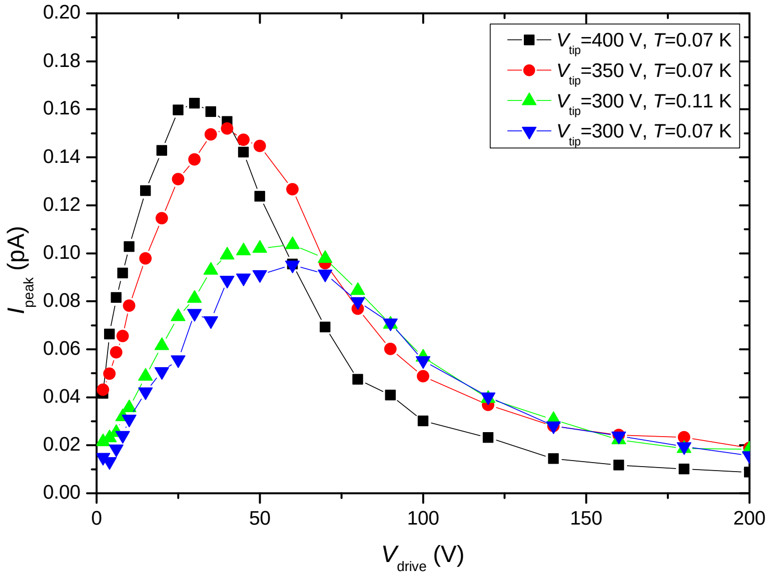

(a) Collector

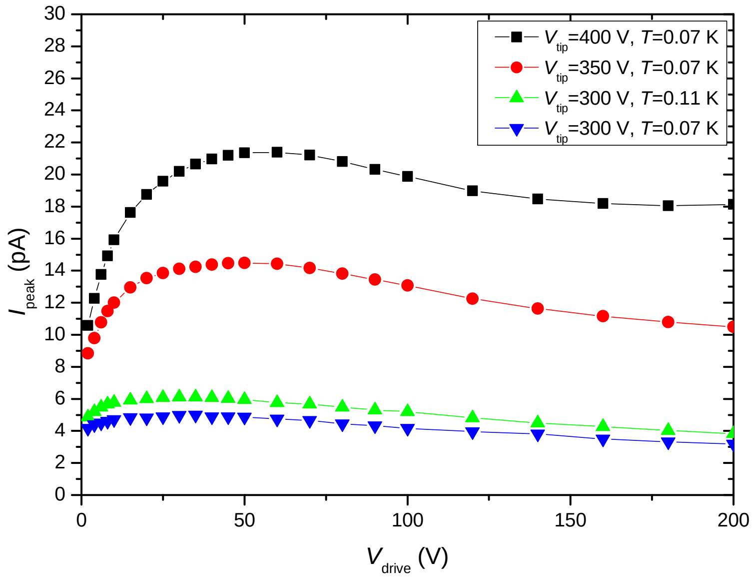

(b) Mid-plate

Figure 2.9: Magnitude of the peak current received by (a) the collector and (b) the mid-plate at each drive voltage for pulse length of 0.05 s.

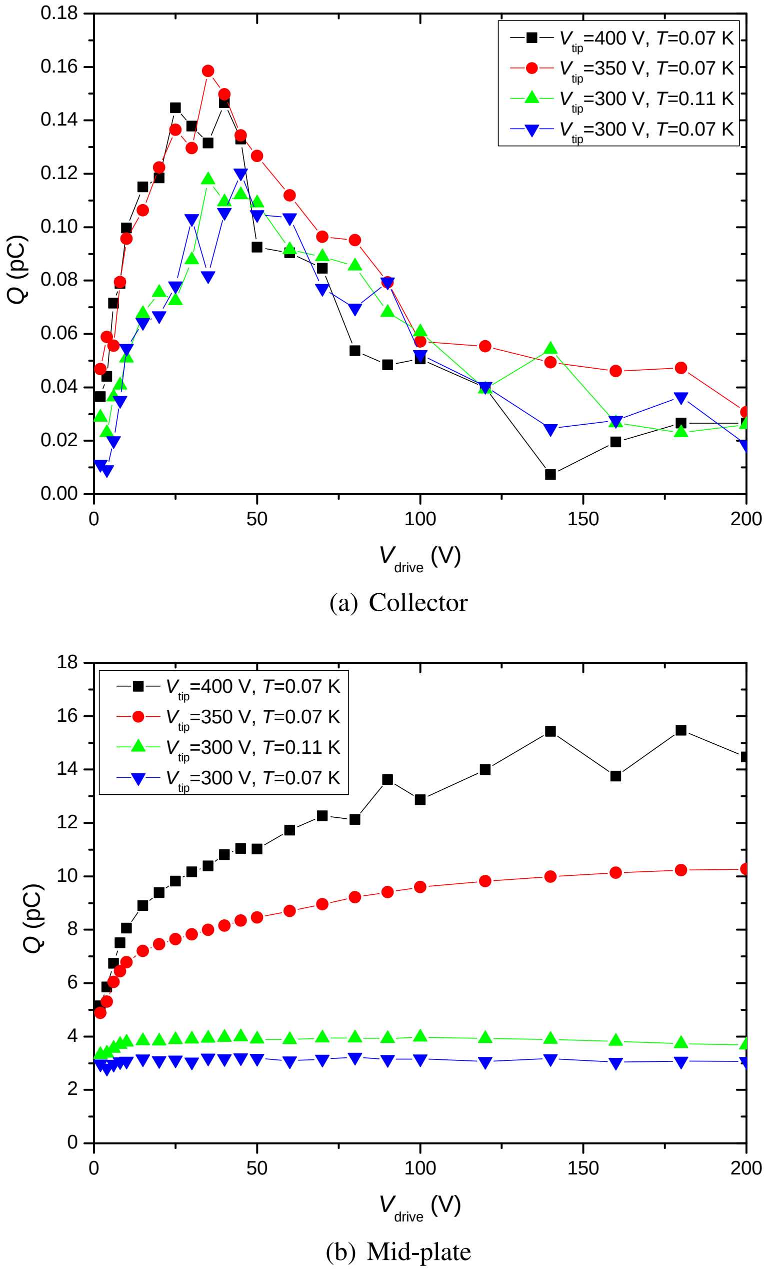

(a) Collector

(b) Mid-plate

Figure 2.10: Charge accumulated on (a) the collector and (b) the mid-plate, obtained by integrating the current data from 0 to 4 s, against the drive voltage for pulse length of 0.05 s.

Figure 2.11 offers a comparison of the total charge fired into the cell from 0 to 4 s between the two cases with pulse length of 0.05 s and of 0.10 s. The total charge, Q_{total}, is derived by summing the charge received by the mid-plate, Q_{mp}, the Frisch grid, Q_{g}, the top plate, Q_{tp} and the collector, Q_{c}. It is dominated by the charge on the mid-plate, since the charge on the other channels is orders of magnitude smaller. Longer pulse length does result in more CVRs injected into the experiment, but the magnitude does not double as the pulse length does. The increase in the total charge for longer pulse length is more obvious for larger tip voltage. It can be concluded that the tip voltage is important in pushing CVRs into the cell. The slow increase in the total charge, which is more obvious at higher tip voltage, suggests that the drive voltage also has some effect on this, but probably not as huge as we would assume.

Since the beam of CVRs injected into the cell has a width much larger than the size of the hole in the mid-plate, a large number of rings are stopped by the mid-plate. The position of a vortex ring arriving at the mid-plate determines whether it is able to make through the hole. This was looked into by running simulations on the dependence on the drive voltage and on the initial injecting direction of the ring. A ring is injected into the experimental cell at an elevation angle from 0 ° to 90 ° in the steps of 1 ° while the azimuth angle is kept at 0 °. The drive voltage is varied from 2 V to 200 V, in accordance with the experiment. Due to the symmetry of the experimental cell, we are only looking at half of the cell. The hole ranges from $x = 0$ to $x = 2.5$ mm and the cell wall is at $x = 22.5$ mm.

The trajectories of the ring in the xz-plane at every $10\,^{\circ}$ for drive voltages of 2 V and 30 V are provided in Figure 2.12, with positions of the mid-plate, the hole rim and the cell wall indicated by arrows in (a). When the drive voltage is low, e.g., at 2 V, only rings injected at elevation angle higher than 75 ° can go through the hole, making a passing rate of 16.5 % out of the 91 angles of injection. Stronger electric field aligns the rings to its direction faster and thus the width of the vortex ring beam quickly

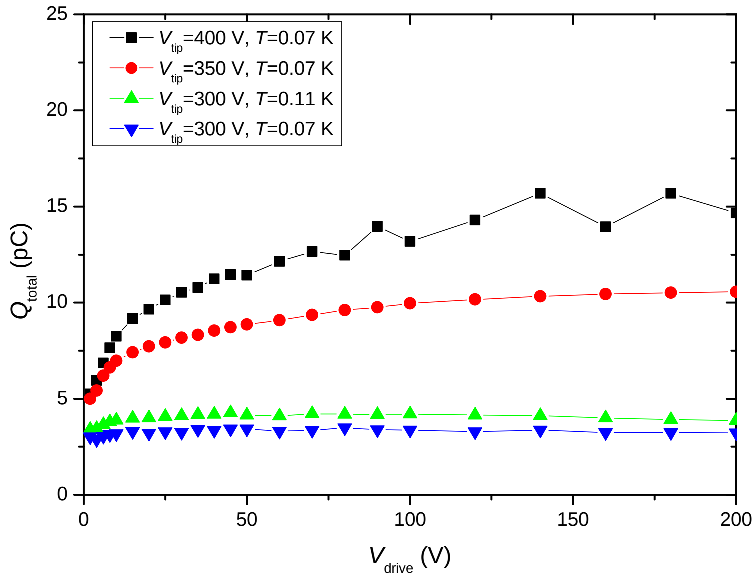

(a) 0.05 s

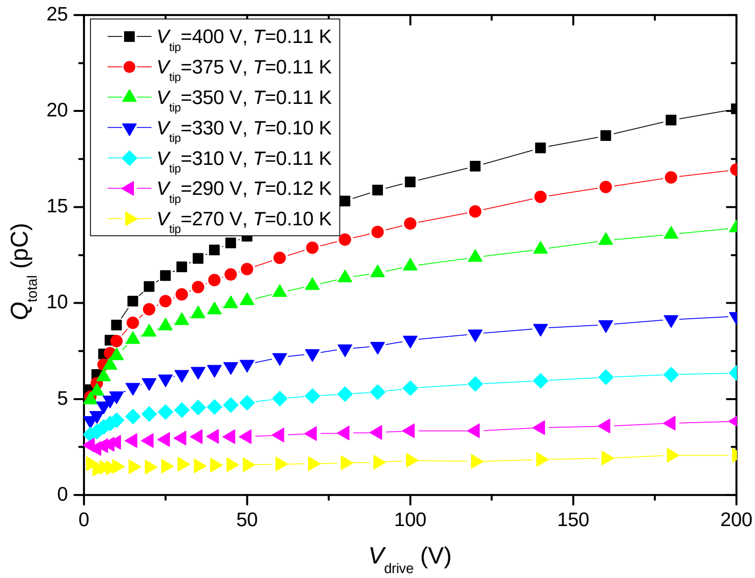

(b) 0.10 s

Figure 2.11: Total charge injected into the experimental cell from 0 to 4 s for pulse length of (a) 0.05 s and (b) 0.10 s, derived by summing up the integration of the current transients on the four channels, $Q_{\mathrm{total}} = Q_{\mathrm{mp}} + Q_{\mathrm{g}} + Q_{\mathrm{tp}} + Q_{\mathrm{c}}$.

reduces. At 30 V, even rings injected horizontally travel through the hole. At drive voltage above 30 V, we should expect that all rings are able to travel beyond the mid-plate. However, experimental results in Figure 2.10 show that the number of the CVRs reaching the collector drops rapidly above 50 V, which suggests that the interactions induced by high drive voltage produces larger spread of CVRs and the ratio of the rings through the mid-plate drops.

We are curious about the proportion of CVRs that are actually able to travel through the hole during the experiment. From previous current plots, the current on the mid-plate is orders of magnitude larger than on any other channel. Dividing the charge on the three channels other than the mid-plate by the total charge emitted into the cell gives us this ratio $r_{\text{through}} = \left(Q_{\text{g}} + Q_{\text{tp}} + Q_{\text{c}}\right)/Q_{\text{total}}$. From Figure 2.13, r_{through} starts at about 0.02 and experiences an increase for low drive voltages until 50 V. After that, the ratio slowly decays. At the same drive voltage, lower tip voltage enables more rings to come through the mid-plate. The highest percentage of rings through the mid-plate does not exceed 10% and is reached at around 50 V. According to the analysis on the width of the peak, this voltage is also where the distribution of ring radii is the narrowest, which could have made it easier for rings to travel beyond the hole.

Due to the interactions between vortex rings, many CVRs would deviate from their initial directions and arrive at the top plate rather than the grid and the collector located in the centre of the plate. A ratio of transverse spread is defined as $r_{\text{spread}} = Q_{\text{tp}}/\left(Q_{\text{tp}} + Q_{\text{g}} + Q_{\text{c}}\right)$ to roughly describe the range of the CVRs that eventually reach the top of the cell. As seen in Figure 2.14, the ratio starts off with a value of about 0.2 then experiences a dip before goes up again to as high as 0.6 with increasing drive voltage. The width of the vortex ring beam has become much larger at higher drive voltage, indicating the increase in interactions. For the same drive voltage, higher tip voltage leads to wider spread of the charge. At drive voltage of 50 V, the narrow spread of charge, together with the highest successful rate of passing through the mid-plate, results in the largest number of CVRs reaching the collector and thus maximum amount of charge is received at 50 V as shown in Figure 2.10 (a).

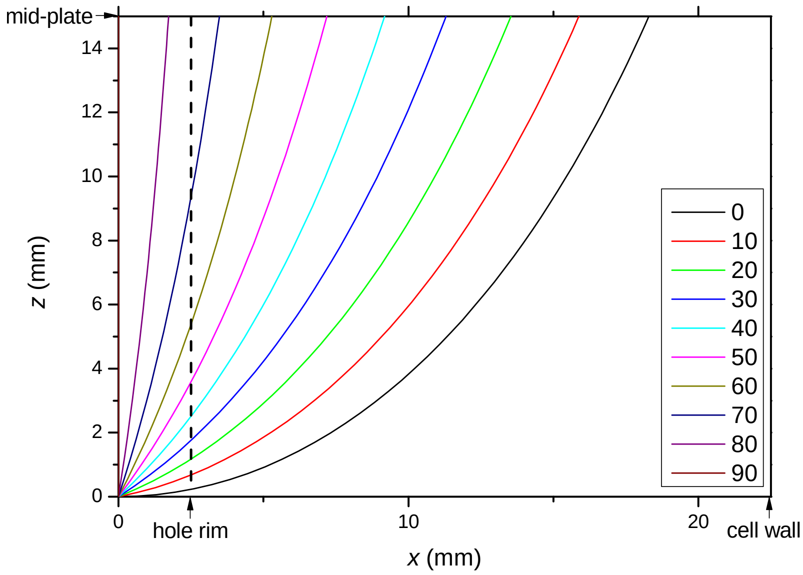

(a) 2 V

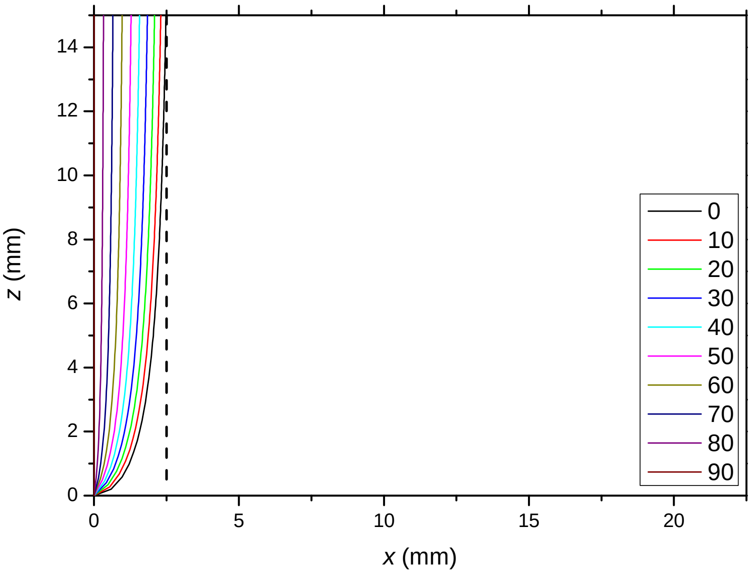

(b) 30 V

Figure 2.12: Projection of the trajectories of the vortex ring in the xz-plane injected with elevation angle from 0° to 90° in the steps of 10°, at drive voltages of (a) 2 V and (b) 30 V. The beam of vortex rings narrows with the increasing drive voltage, making the ring injected at all angles through the hole at 30 V.

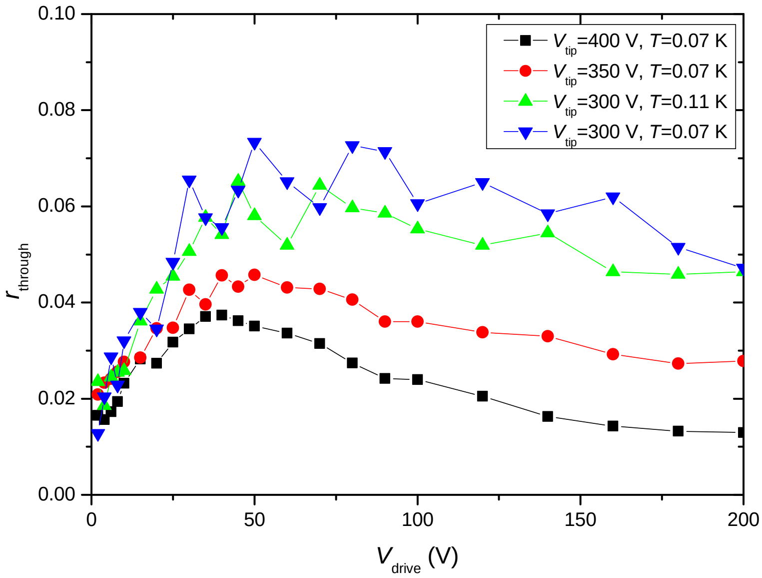

Figure 2.13: Ratio of rings that have travelled through the hole in the mid-plate for pulse length of 0.05 s, calculated as $r_{\text{through}} = (Q_g + Q_{tp} + Q_c)/Q_{\text{total}}$.

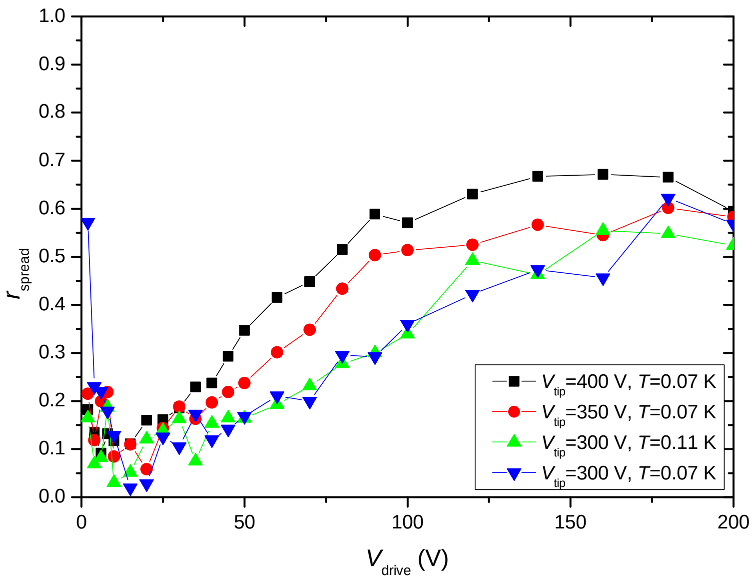

Figure 2.14: Transverse spread of charge on the top plate for pulse length of 0.05 s, derived as $r_{\text{spread}} = Q_{tp}/(Q_{tp} + Q_g + Q_c)$.

With the Frisch grid in front, not all CVRs travelling towards the centre of the top plate are able to reach the collector. Hence, the effective transparency of the grid, T_g, with regard to the voltage is investigated. As mentioned in Section 2.1, the grid has a wire mesh with a geometric transparency of 92%. However, in the experiment, the

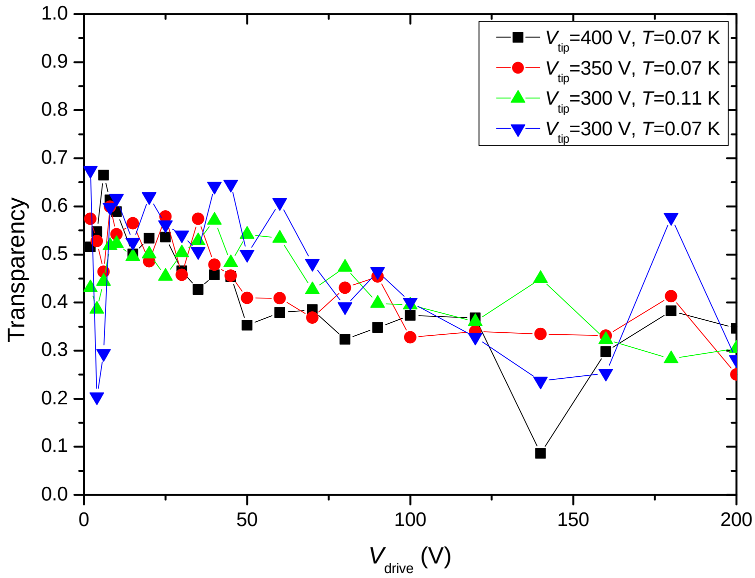

Figure 2.15: Effective transparency of the Frisch grid, defined as $T_{\mathrm{g}} = Q_{\mathrm{c}}/\left(Q_{\mathrm{c}} + Q_{\mathrm{g}}\right)$, for data with pulse length of 0.05 s.

current on the mesh cannot be separated from the current on a metal ring that the mesh is attached to. The current on the Frisch grid actually refers to the total current on both the mesh and the ring and the ring has no transparency at all. Taking the size of the ring into consideration, the transparency is expected to be around 0.6. The experimental transparency is defined as the charge accumulated on the collector divided by the total charge on both the collector and the Frisch grid, $T_{\mathrm{g}} = Q_{\mathrm{c}}/\left(Q_{\mathrm{c}} + Q_{\mathrm{g}}\right)$, and is presented in Figure 2.15. From the plot, the transparency starts at approximately 0.55 at low drive voltages, which agrees with our expectation. Then it goes down slowly as the drive voltage becomes higher and reaches 0.3 at 200 V. As confirmed by the ratio of spread on the top plate, the beam of CVRs becomes less-collimated at higher drive voltages. More rings will end up on the metal ring and the decline of transparency is expected. The tip voltage does not show much impact on the result.

In the comparison between the analysis results for data with pulse length of 0.05 s and of 0.10 s, the only significant difference is that more CVRs are injected into the cell when the pulse length is doubled, leading to an increase in the current and the charge data. The properties of the charged vortex tangle near the injection tip are not affected by the pulse length since the release time of the CVRs and the width of the current peak for the mid-plate data have approximately the same constant values in both cases. Other physical parameters, such as the ratio of rings through the mid-plate, the transverse spread and the transparency of the grid, do not display strong dependence on the pulse length either.

2.4 Temperature Dependence

Measurements were carried out while the tip voltage was kept at 350 V to check the temperature dependence. The pulse length was 0.05 s. The drive voltage was switched between six values: 10 V, 20 V, 30 V, 40 V, 60 V and 100 V. The temperature went from as low as 0.08 K to as high as 0.70 K in small steps. The currents received on each channel are processed the same way as for the voltage dependence data. The analytical time of flight was computed for every experimental temperature for each of the six drive voltage values using Equations 2.11 and 2.15. The most appropriate value of the constant logarithm term Λ for the calculations was found to be 11, corresponding to a radius of 0.97 μm.

Peak time and time at the edge of the peak for currents on the mid-plate with regard to temperature are given in Figure 2.16, which are reflective of the time scales of the seed CVRs entering the cell. t_{edge} has a value of about 0.07 s throughout the temperature range of the experiment. This value 0.07 s is close to the average of 0.08 s that we obtained for the voltage dependence case with the same 0.05 s pulse length, revealing that the release time of the seed CVRs from the tangle near the tip is not much affected by temperature or the voltage. t_{peak} stays at about 0.3 s and only goes up to a small degree at high temperatures. Thus, the properties of the charged tangle near the injection tip do not present a strong temperature dependence.

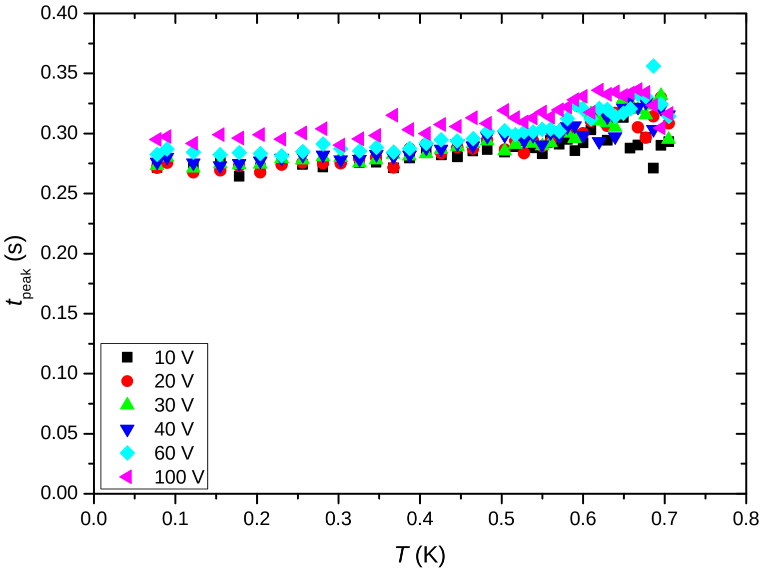

(a) Peak time

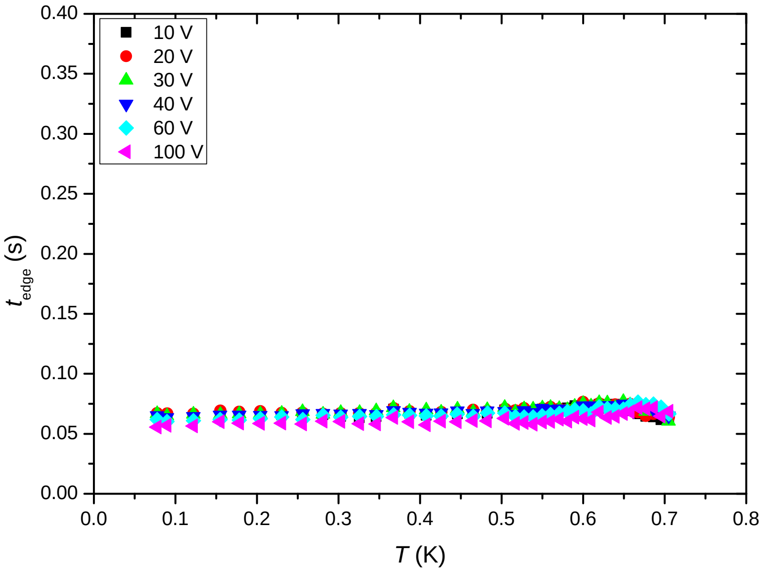

(b) Time at edge

Figure 2.16: (a) Peak time and (b) time at the edge of the peak of the currents received by the mid-plate versus temperature, for pulse length of 0.05 s. $t = 0$ starts from the middle of the pulse. The tip voltage was kept at 350 V and the temperature was varied from 0.08 K to 0.70 K in small steps.

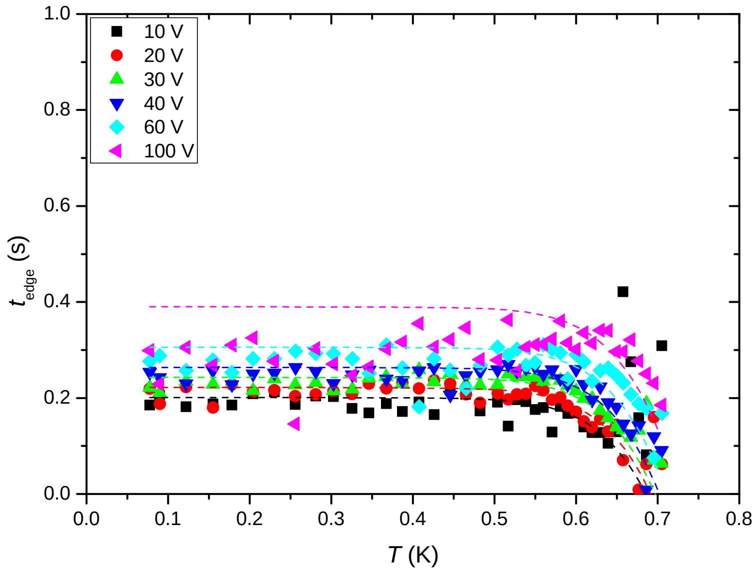

Figure 2.17: Time at the edge of the peak for currents from the top plate versus temperature. The dashed curves are the analytical time of flight for a CVR of initial radius 1.0 μm to reach the mid-plate at different drive voltages. The logarithm term Λ in Equation 2.11 is set to have a constant value 11.

Time at the edge of the peak for currents from the top plate can be translated as the time that induced currents are received by the detector, i.e., the time that the CVRs successfully pass through the mid-plate, and is shown in Figure 2.17. t_{edge} remains almost constant with small fluctuations until 0.5 K and quickly decreases to almost zero at 0.7 K. The experimental data are compatible with the analytical time of flight to the mid-plate for a CVR with initial radius of 1.0 μm at different drive voltages, which is calculated using Equation 2.11. At the same temperature, the higher the drive voltage is, the longer it takes for the rings to travel past the mid-plate.

Figure 2.18 shows the peak time and time at the edge of the peak for the collector data with respect to temperature. Since the first group of CVRs to arrive at the collector should be the smaller rings created during reconnections, t_{edge} is compared to the analytical time of a CVR with initial radius of 0.5 μm using Equation 2.15 and those rings appear to have radii even smaller than 0.5 μm. t_{peak} is plotted with analytical calculation for a ring of 1.0 μm. Both sets of data are independent of temperature until the temperature reaches 0.5 K, then decrease slightly before climbing up again. The gradient of the analytical calculation agrees with the experimental data till around 0.6 K, when the experimental time starts to go up and the analytical time drops to zero. The occurrence of the unphysical zero analytical time of flight results from the shrinking of the ring under the large mutual friction at high temperatures. The reason for the sudden rise in the experimental time of flight is that the small rings are quickly dissipated due to mutual friction, leaving behind a stationary bare ion in the field-free region which might never reach the collector; whereas the large impulse of the tangles allows them to make it to the collector eventually.

The widths of the current peaks for the collector and the mid-plate are presented in Figure 2.19. For the mid-plate data, t_{width} has an almost constant value of 0.4 s before slightly increasing at temperature above 0.6 K, which means the difference in the radii of the arriving CVRs on the mid-plate is not much dependent on the increasing temperature. This again shows that temperature does not have much impact on the release of the CVRs from the tangle near the tip. For the collector data, the magnitude is kept constant at about 0.6 s but climbs up after the temperature reaches 0.6 K. This observation confirms the assumption that at high temperatures above 0.6 K, instead of isolated vortex rings, the charge is carried by large vortex tangles which move at a low velocity.

The peak current on the collector and the mid-plate from 0.08 K to 0.70 K for each drive voltage is given in Figure 2.20. In general, the curves exhibit a downward trend but begin to drop faster after 0.5 K. For the collector, it almost drops to zero at 0.7 K, which indicates there are very few charge carriers that are able to travel across the cell at high temperatures. The mid-plate data is approximately two orders of magnitude higher than the collector data since a large number of CVRs cannot travel beyond the hole in the plate due to the width of the beam. At drive voltages between 10 V and 40 V, for the same temperature, the peak current increases with the increasing drive

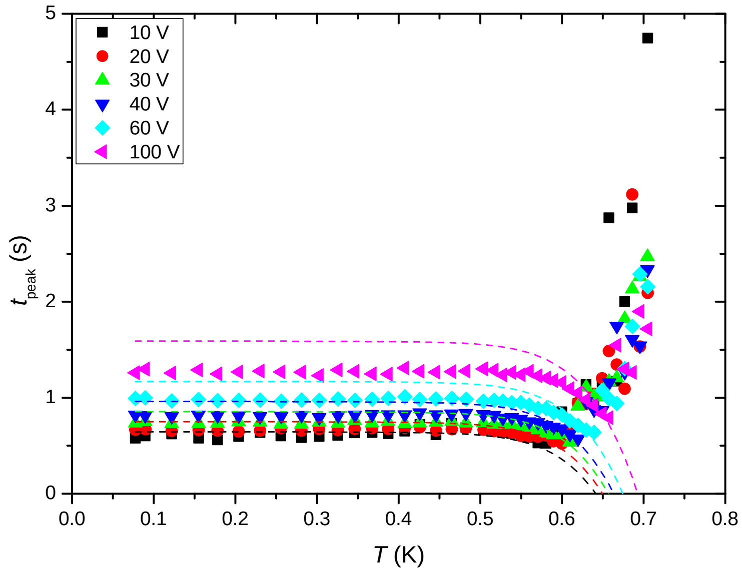

(a) Peak time

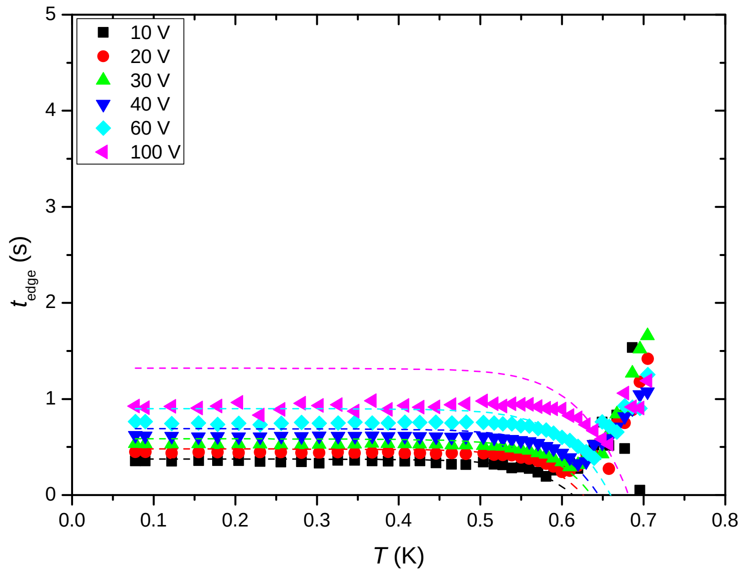

(b) Time at edge

Figure 2.18: (a) Peak time and (b) time at the edge of the peak against temperature for the collector, for pulse length of 0.05 s. The time $t = 0$ starts from the middle of the pulse. The dashed curves are the calculated time of flight for a CVR to reach the collector at the different drive voltages, with the initial radius of the ring being 1.0 μm for peak time and 0.5 μm for time at edge. The logarithm term Λ is 11.

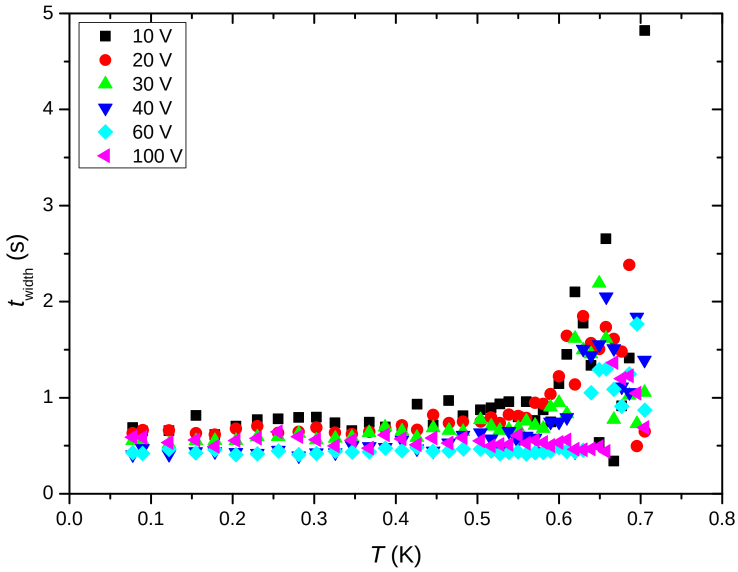

(a) Collector

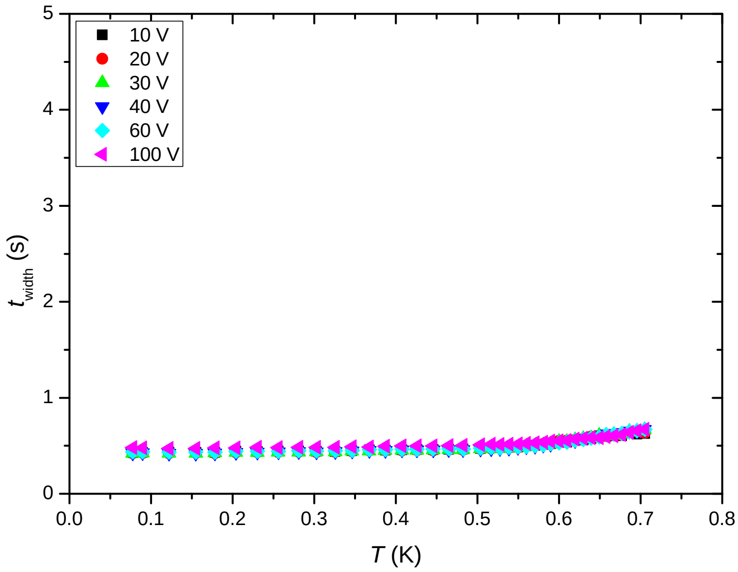

(b) Mid-plate

Figure 2.19: Width of the current peak for (a) the collector and (b) the mid-plate against varying temperature. It is derived by calculating the time interval between the half maximum points of the peak.

voltage, but at higher voltages, the opposite happens. A jump in the peak current is noticed at around 0.3 K, which is caused by a sudden change in the characteristics of the injection tip.

Figure 2.21 displays the charge accumulated on the collector and the mid-plate respectively, derived by integrating the currents on those two channels from 0 to 4 s. The collector data experiences some relatively huge fluctuations in the experimental temperature range but it can still be deduced that generally less charge is received by the collector as the temperature rises. The charge on the mid-plate follows the observation in the peak current analysis: overall, it is decreasing, with a jump in magnitude at 0.3 K due to a faulty injection tip. Above 0.5 K, small rings are quickly dissipated under the influence of the mutual friction, which accounts for the rapid decrease in the accumulated charge at high temperatures.

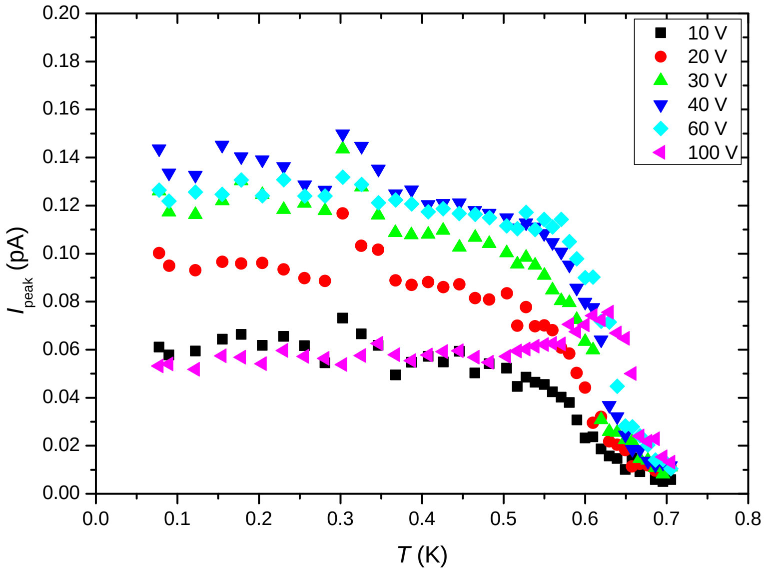

(a) Collector

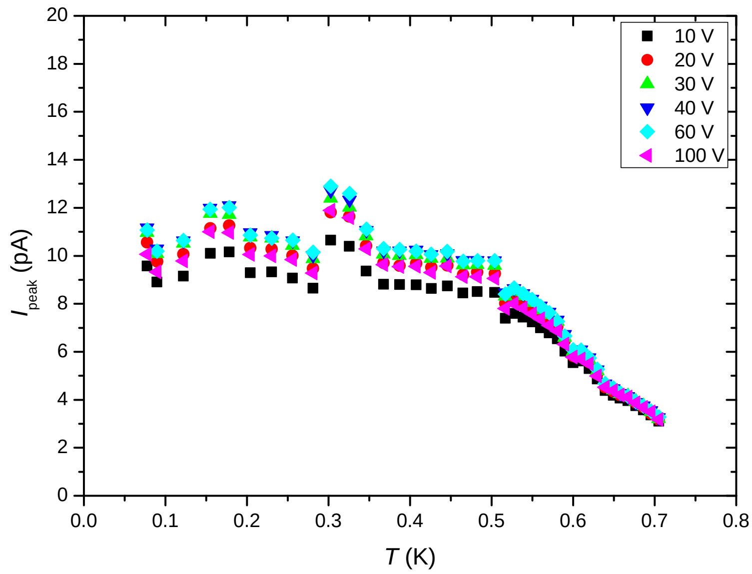

(b) Mid-plate

Figure 2.20: Peak current received by (a) the collector and (b) the mid-plate at each temperature varying from from 0.08 K to 0.70 K. The noticeable jump at around 0.3 K is due to a sudden change in the characteristics of the injection tip.

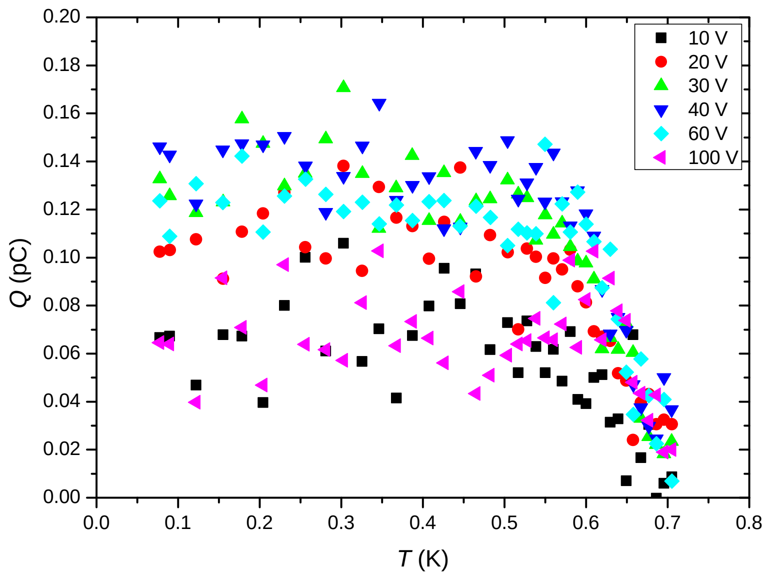

(a) Collector

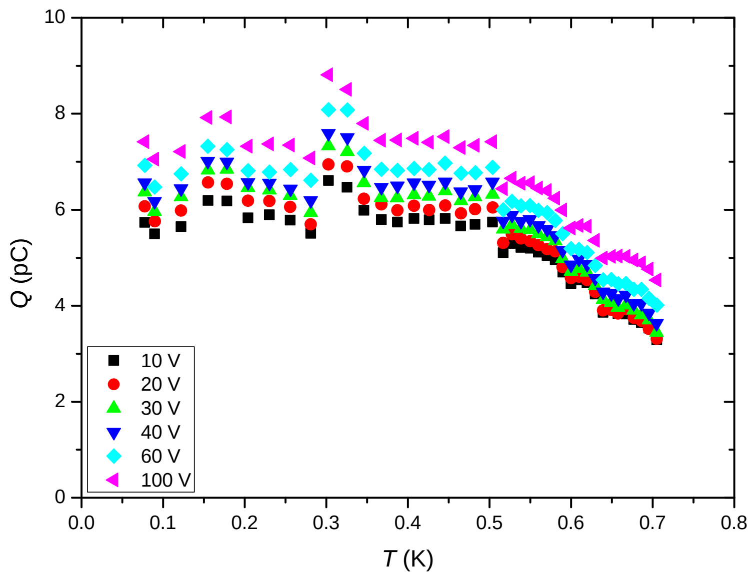

(b) Mid-plate

Figure 2.21: Charge accumulated on (a) the collector and (b) the mid-plate versus temperature at six different drive voltages, derived from integrations of the current transients from 0 to 4 s.

Chapter 3

Double Ring Collision

3.1 Introduction

The interactions between a pair of vortex rings can provide information on the processes that occur in quantum turbulence at microscopic scales, such as reconnections between rings, self-reconnections and the transfer of energy to Kelvin waves. One important example is that the generation of much smaller vortex rings observed during experiment could be tested through simulation on vortex ring reconnections. A lot of research work has been devoted to the interacting and reconnecting vortex rings, as reviewed in Chapter 1. In this chapter, we provide a detailed study of the interactions between two vortex rings, both circular and deformed, initially travelling in the same direction. The chapter starts with a discussion of the case of two circular rings in Section 3.2, then we look into the interactions between rings with manually imposed perturbation in Section 3.3, and with deformation generated from ring collision in Section 3.4.

In superfluid ^{4}He, the vortex core radius a is much smaller compared to any other characteristic length scale such as the radius of the vortex ring R, which makes the vortex filament method appropriate for our simulations on the interactions between vortex rings in superfluid ^{4}He. Although local induction approximation is computationally cheaper, it does not cover the long-range non-local effects between the vortex rings. Therefore the exact Biot-Savart law is employed for all our simulations.

A C++ program was developed, initially by Matthew Evans and Rory Brown, to fulfill our simulation on the dynamics of a pair of vortex rings in superfluid helium, using the vortex filament method and the full Biot-Savart law. A characteristic length of the ring segments, δ, is introduced to maintain the resolution of the filaments. This length is chosen to be $\simeq 6 \times 10^{-8}$ m such that a ring of 1 μm radius comprises of $\simeq 100$ mesh points, where 1 μm is in accordance with the typical order of magnitude of the size of the vortex rings observed in superfluid helium experiments [20]. We follow Baggaley and Barenghi [35] by using an adaptive meshing to maintain the resolution of the simulation. If the separation between two neighbouring points exceeds δ, a new point is added in between; if any ring segment is below $\delta/2$ in length, a point is taken out. In the event that the local curvature at any mesh point surpasses $1.9/\delta$, that point is removed to smooth out the filament, which results in a small loss of line length and energy. This process is thought to crudely mimic the phonon emission for Kelvin waves with large wavenumber occurring at zero temperature limit [35]. In order to account for the variation in mesh sizes along the vortex filaments, all spatial derivatives are approximated using a fourth-order finite difference schemes given by Baggaley and Barenghi [35]. The derivatives of the ith point $\boldsymbol{s}_i'$ and $\boldsymbol{s}_i''$ have a dependence on the positions of the two points in front and the two points behind. Since the calculation involves at least 5 mesh points, any ring with less than 6 mesh points is not allowed to exist and must be eliminated from the simulation.

Time evolution is achieved using the fourth-order Adams-Bashforth scheme (AB4). For a mesh point i with velocity $\boldsymbol{v}_i$, the calculation of its position $\boldsymbol{s}_i$ at time step $n+1$ involves velocities from four prior time steps:

$$\boldsymbol{s}_i^{n+1} = \boldsymbol{s}_i^n + \frac{\Delta t}{24}\left(55\boldsymbol{v}_i^n - 59\boldsymbol{v}_i^{n-1} + 37\boldsymbol{v}_i^{n-2} - 9\boldsymbol{v}_i^{n-3}\right), \tag{3.1}$$

where Δt is the time step with magnitude of $\simeq 10^{-10}$ s in our simulations. During the initialisation of a new mesh point, whether at the beginning of the entire simulation or afterwards when a new point is called for, its velocity at the first four time steps is determined according to lower-order schemes, i.e., Euler, AB2 and AB3.

The vortex filaments in superfluid helium are expected to reconnect when they become sufficiently close to each other. In our simulations, reconnection algorithm must be supplemented manually to the vortex filament model. Baggaley [50] provided a detailed comparison on the effects of various reconnection models. When the distance between two non-adjacent mesh points drops below a critical distance $\Delta = \delta/2$, a reconnection is initiated. Following Baggaley [50], we employ one of the simplest reconnection algorithms denoted by *Type II*. A schematic plot for the reconnection process in presented in Figure 3.1. If two points fall within distance Δ, they simply reconnect and the other points in the vicinity of those two points are reassigned accordingly. No dissipation algorithm is considered at this stage. To ensure that only anti-parallel filaments will reconnect, the inner product of the positions of the two reconnecting points is checked and the reconnection proceeds only when negative value is obtained. Further details on the implementation of the vortex filament method can be found elsewhere [51].

To better compare the sizes of the CVRs with minimal impact from ring deformation, an effective radius, R_{eff}, is defined to give the radius of a smoothed version of the deformed ring, which is an equivalent circular ring with the same momentum but without the Kelvin waves. This is valid provided the deformation on the ring is small. The effective radius can be derived from computing the impulse, $P = \pi\kappa R_{\text{eff}}^2$, where the definition of the impulse is [52]

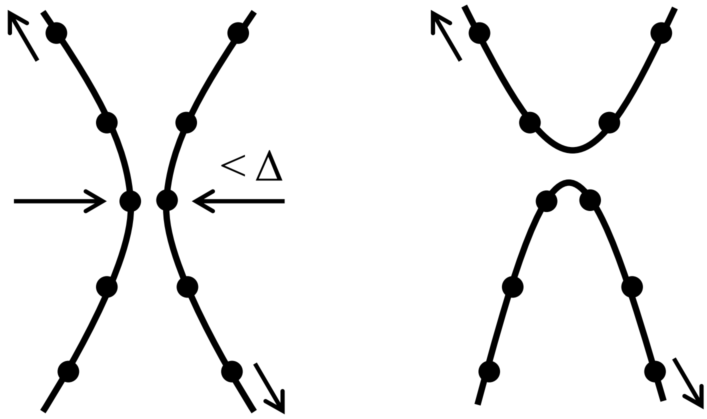

Figure 3.1: Reconnection of two anti-parallel vortex filaments. The black dots represent the mesh points on the filament, and the orientation is indicated by the little arrows. The plot on the left shows the configuration before reconnection, and the reconnection result is on the right.

$$\boldsymbol{P} = \frac{1}{2}\rho\kappa \sum_i \boldsymbol{r}_i \times \boldsymbol{\xi}_i, \tag{3.2}$$

for i from 0 to the total number of mesh points on that ring, with $\boldsymbol{r}_i$ being the position vector and $\boldsymbol{\xi}_i$ the length of the vortex segment.

Analysing the components of the total energy can provide insight on the interactions between vortex rings. We assume that the Kelvin waves on the vortex rings in our simulations have small enough amplitude, such that the effective smoothed ring moves in the same direction as the original deformed ring. The total energy of a system of vortex rings can be seen as having contributions from two main sources,

$$E_T = E_{\text{ring}} + E_{\text{KW}}, \tag{3.3}$$

where E_{ring} is the energy of the smoothed rings and E_{KW} is the energy stored in the distortion caused by Kelvin waves on the ring. Performing line integral $E = \rho\kappa \oint \boldsymbol{v_s} \cdot \boldsymbol{s} \times \hat{\boldsymbol{s}}' \mathrm{d}\xi$ [52] proves that the total energy is conserved within $0.1\ \%$ during the simulation and that the decrease in energy after reconnections can be neglected. The energy fractions with regard to the total energy are expressed as

$$\frac{E_{\text{ring}}}{E_T} = \frac{1}{R_1 + R_2} \sum R_{\text{eff}} \tag{3.4}$$

$$\frac{E_{\text{KW}}}{E_T} = 1 - \frac{E_{\text{ring}}}{E_T} = 1 - \frac{1}{R_1 + R_2} \sum R_{\text{eff}}. \tag{3.5}$$

Here, the summation is over all existing rings.

3.2 Circular Rings

The first scenario to be explored is when two perfectly circular vortex rings with radii R_1 and R_2 ($R_1 \geq R_2$) initially moving in the z-direction interact. The axes perpendicular to the ring planes are offset by an impact parameter, b, which was varied to test the effect of relative position on the interactions. The ring with larger initial radius R_1 is always placed before the smaller one with a distance of d, so the coordinates of the centres of the two rings at the beginning of the simulation are $(0, 0, d)$ and $(b, 0, 0)$. Since the ring velocity is proportional to the inverse of the radius, the smaller ring in the back is able to catch up with the larger one and the non-local interactions between them can initiate a series of reactions depending on the impact parameter. The separation d is set to be 5 μm, which is a safe distance for the two rings to be approximated as independent and non-interacting at the start. The simulations were performed for a duration of $\simeq$ 1 ms, allowing enough time for the rings to interact and evolve to a final state where the rings are far apart.

An interesting configuration to study is when $R_1 = 1.2\,\mu$m and $R_2 = 0.7\,\mu$m. Figure 3.2 shows sequences of snapshots for two examples of the interacting vortex rings, each with three frames. The smaller ring has a larger velocity and sets off to catch up with the larger ring in front as soon as the simulation starts. The long-range interaction causes the ring in front to expand and the one behind to shrink in size.

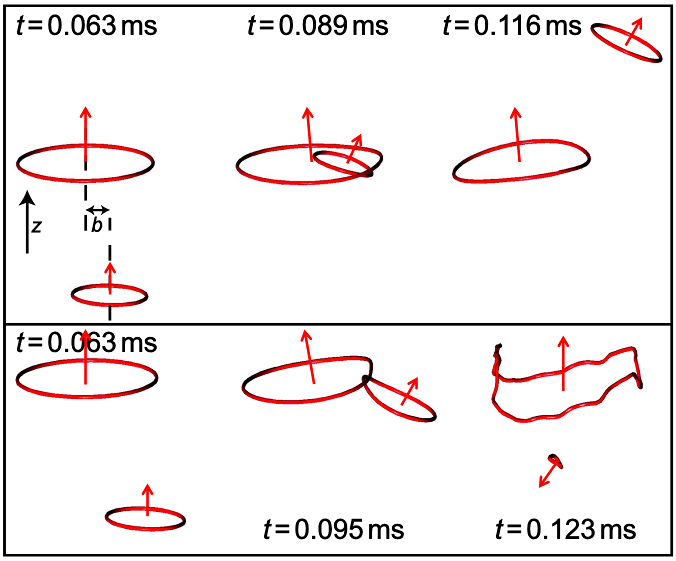

Figure 3.2: Snapshots for the interactions of two different sets of vortex rings, evolving with time from left to right as indicated. Same initial conditions are applied: rings start off $5\,\mu$m apart and travel in the z-direction, with initial radii $R_1 = 1.2\,\mu$m and $R_2 = 0.7\,\mu$m. The red arrows indicate the directions of the ring velocities. Top panel: for impact parameter $b = 0.4\,\mu$m, the smaller ring safely passes through the larger one without reconnection. Bottom panel: for impact parameter $b = 0.95\,\mu$m, both rings reconnect and merge into a single ring, which later self-reconnects and produces a small ring.

This can lead to a leapfrogging motion: if the two rings are initially co-axial, the rings continue to move forward along the z-direction; if not, the rings also tend to push each other sideways. The top panel is an example when the impact parameter ($b = 0.4\,\mu$m) is small enough for the smaller ring to pass through the other one without reconnecting, leaving both rings deformed and deviated from previous direction due to interactions. In the bottom panel, a larger impact parameter ($b = 0.95\,\mu$m) is applied and reconnection is observed. The vortex rings collide after approaching each other and reconnect, merging into one large deformed loop, which then self-reconnects and generates a small ring. The deformation seen on the large loop results from the Kelvin waves created from reconnection.

After each run, the momenta of all remaining rings are calculated using Equation 3.2 and the effective radii, R_{eff}, are derived to compare the results of the interactions. Since the circular rings are symmetric about both x and y axes, the interactions at different impact parameters should also have the same symmetry about the axes. The final effective radii are plotted in Figure 3.3 with respect to the impact parameter b in $+x$ direction, which is reflective of the ring interaction outcomes in all other directions. Based on the types and the results of the interactions that have taken place between the two rings, the whole range of impact parameters is separated into four different regimes by three b values b_1, b_2, b_3, marked as the vertical dashed lines in the figure. The window of impact parameters for ring reconnection is $b_1 \leq b \leq b_3$.

For $b < b_1$, the lower ring passes through the upper one from inside without reconnecting, as demonstrated in the top panel of Figure 3.2. Compared to the initial radii, the changes in the final effective radii of the two rings are limited, although both rings are left with certain deformation. The movements of the rings slightly deviate from the initial strictly upward direction due to sidewards interactions.

When $b_1 \leq b < b_2$, the second ring collides with the first ring on the side. They reconnect and produce one smaller and one larger rings. The difference between the final R_{eff} of the rings grows as b increases. Close to the boundary b_2, the smaller ring produced is nearly 4 times smaller than the initial one, which offers potential explanation for the sources of the very small rings observed during experiments.

When $b_2 \leq b \leq b_3$, the rings reconnect and then merge into one large deformed loop, as shown in the bottom panel of Figure 3.2. Sometimes this deformation is strong enough for a small ring to be emitted later due to loop self-reconnection. From the conservation of momentum and Equation 1.8, the maximum radius of the loop formed by the merging is given by $R_{\text{max}} = \sqrt{R_1^2 + R_2^2} \approx 1.39\,\mu\text{m}$, which agrees with our simulation results and shows that momentum is indeed conserved in our simulations.

For $b > b_3$, the lower ring slides from below the upper one to miss it on the outside

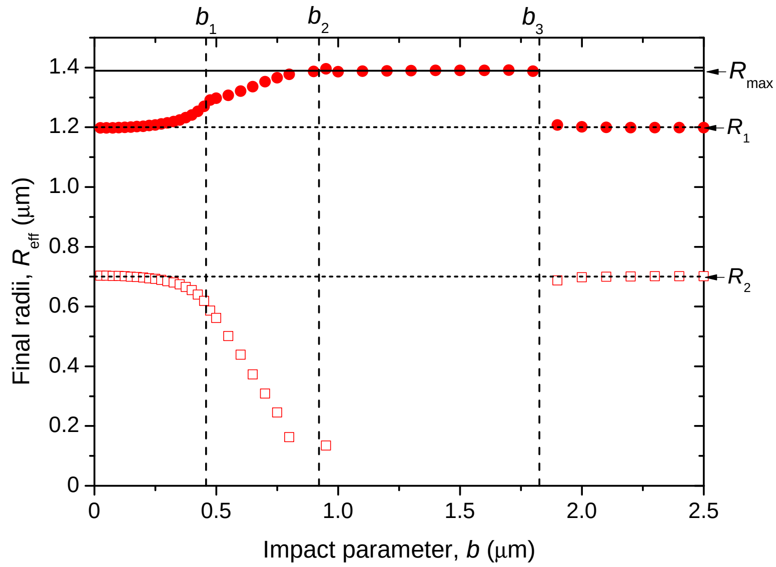

Figure 3.3: Final effective radii of the rings, R_{eff}, against the impact parameter, b. The solid symbol is for the larger ring and the open symbol is for the smaller one. The initial conditions include $R_1 = 1.2\,\mu$m and $R_2 = 0.7\,\mu$m, which are indicated by the horizontal dashed lines, with the first ring placed $d = 5\,\mu$m above the second one. The impact parameters are divided into 4 regimes by b_1, b_2, b_3, based on the results of interactions between the rings. Ring reconnection occurs in the region $b_1 \leq b \leq b_3$. $R_{\text{max}} = \sqrt{R_1^2 + R_2^2} \approx 1.39\,\mu$m is the maximum radius expected for the single ring formed by the merging of the initial vortex rings, derived from the conservation of momentum.

with no reconnection observed. There is barely any deformation on the rings afterwards and the final effective radii R_{eff} are almost identical to the initial radii. Without the vortex ring interactions, the upper limit of the impact parameter for ring reconnection should be the sum of the initial radii, $b^{\text{rec}}_{\text{max}} = R_1 + R_2 = 2.1\,\mu$m. However, the simulations suggest that $b_3 < b^{\text{rec}}_{\text{max}}$, because of the sidewards repulsion between the rings.

The transfer of energy between each component of the total energy versus the impact parameter b is shown in Figure 3.4. The three boundaries (b_1, b_2, b_3) in the final radii plot still serve as the regime separators in this case. For $b < b_1$, the rings remain almost circular after interaction, thus E_{KW} is negligible. In region $b_1 \leq b < b_2$, the rings reconnect, which results in the decrease of the energy of the smoothed ring E_{ring},

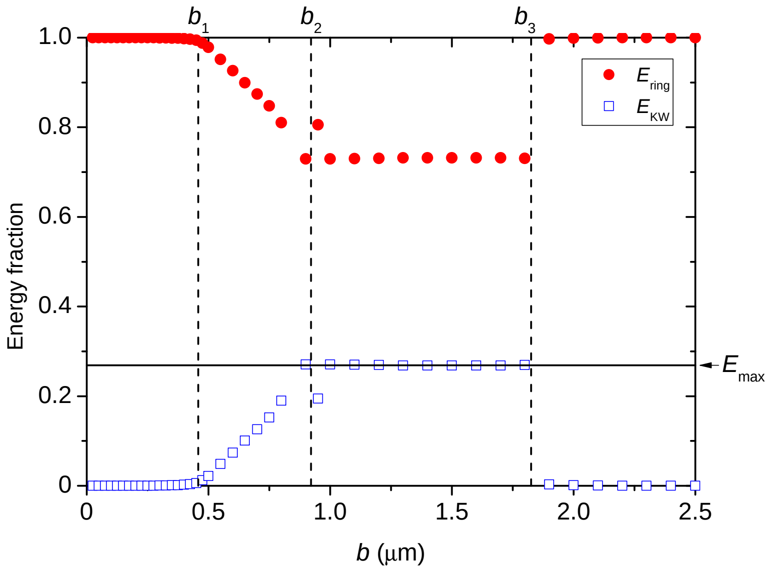

Figure 3.4: Fraction of each energy component (E_{ring} and E_{KW}) compared to the total energy against the impact parameter, for the interactions between two circular rings with $R_1 = 1.2\,\mu$m and $R_2 = 0.7\,\mu$m. Based on the interactions between the rings, the three dashed vertical lines marked by parameters b_1, b_2 and b_3 indicate the boundaries of the four regimes. The solid horizontal line is for the maximum possible fraction of energy stored in Kelvin waves.

and the rising of the Kelvin wave energy E_{KW}. When $b_2 \leq b \leq b_3$, maximum fraction of the total energy is stored in the excited Kelvin waves, as the two rings merge into a largely deformed loop. According to the conservation of energy and momentum, this fraction can be calculated as $E_{\text{max}}/E_T = 1 - R_{\text{max}}/\left(R_1 + R_2\right)$. E_{max} is marked by a solid horizontal line in the figure, which agrees with the simulation results well. For $b > b_3$, the rings fly past each other without much interaction therefore the total energy is nearly all taken up by E_{ring}.

3.3 Manually Imposed Perturbation

In most of the realistic cases, we are not dealing with perfectly circular rings, because the interactions between one vortex ring and another leaves them deformed. One situation that is of special interest to us is when Kelvin waves are imposed on the vortex rings. Barenghi *et al.* [53] proposed a model for the initial conditions of rings with Kelvin waves. The formulae for the perturbation imposed on the vortex rings in our simulations have a slight deviation from theirs. The Cartesian coordinates of each mesh point on the ring can be converted from the cylindrical coordinates (r, ϕ, z) and are expressed as:

$$\begin{aligned} x &= R\sin\phi + A\cos(N\phi)\cos\phi, \\ y &= R\cos\phi + A\cos(N\phi)\sin\phi, \\ z &= -A\sin(N\phi), \end{aligned} \tag{3.6}$$

where A controls the amplitude of the perturbation and N is the number of waves.

We manually impose this kind of perturbation onto a circular vortex ring of initial radius 1 μm while a second circular ring of radius 0.8 μm is initialised at 5 μm below in z direction, and observe their behaviours with respect to the changing impact parameters. The amplitude of the perturbation is expressed as the ratio A/R, which is fixed at 0.05. The deformation of a vortex ring with initial radius of 1 μm at $N = 2$ and 3 is presented in Figure 3.5 for both xy- and xz- planes. Also plotted in dashed curve is the circular ring with the same initial radius. The shape of the ring becomes more irregular with increasing N. The effective radii of the rings can all be regarded as 1 μm, since the deviation is negligible.

The addition of the perturbation changes the motion of the vortex rings. If the ring in front is to travel along $+z$-direction alone without any constraints or interactions, its final position after 1 ms is shown in Figure 3.6. The ring's movement in the z-direction has been hindered, as it travels less with larger N, which is similar to the conclusions obtained by Barenghi *et al.* [53] on the average translational velocity of the vortex ring.

A second vortex ring of radius 0.8 μm is released 5 μm below the first one, also moving upwards in the $+z$-direction. Due to the asymmetric shape of the ring with the imposed Kelvin waves, the impact parameter was varied in both x- and y- directions,

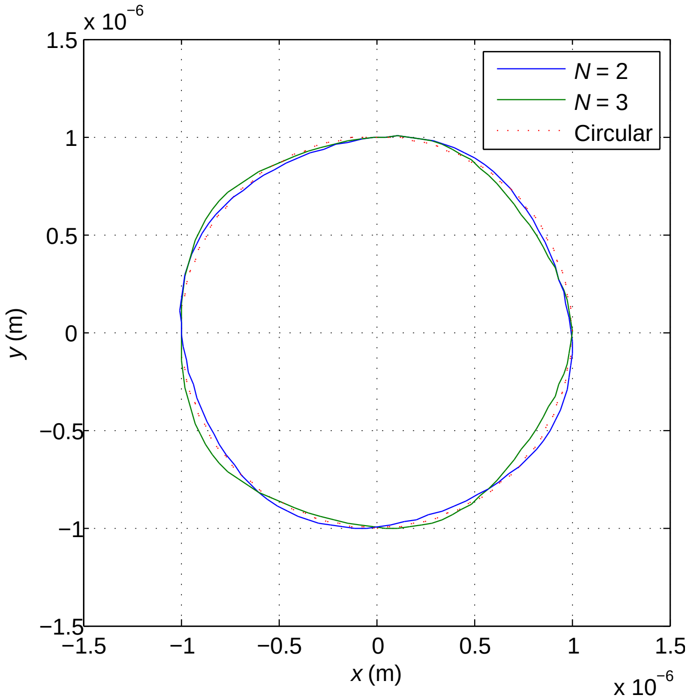

(a)

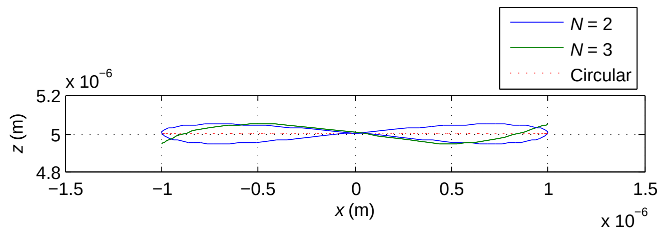

(b)

Figure 3.5: Deformation of a vortex ring of initial radius of 1 μm with perturbation of constant amplitude-to-radius ratios A/R = 0.05 and $N = 2$ and 3, compared to a circular ring of the same initial radius, in (a) xy-plane and (b) xz-plane, at $t = 0$.

denoted by $\boldsymbol{b} = (b_x, b_y)$. Figure 3.7 shows the final effective radii, R_{eff}, of a ring with perturbation of $N = 2$ or 3 after 1 ms versus the impact parameters $(b_x, 0)$ and $(0, b_y)$ respectively, as well as R_{eff} for a circular ring. The plots have the same form as what we obtained in the case of two circular rings with $R_1 = 1.2\,\mu$m and $R_2 = 0.7\,\mu$m ($\Delta R = 0.5\,\mu$m) in Figure 3.3, although the smaller difference in initial radii ($\Delta R = 0.2\,\mu$m) has lead to a narrower region for ring reconnection. The final radii do not exceed the maximum radius allowed for this setup, $R_{\max} = 1.28\,\mu$m.

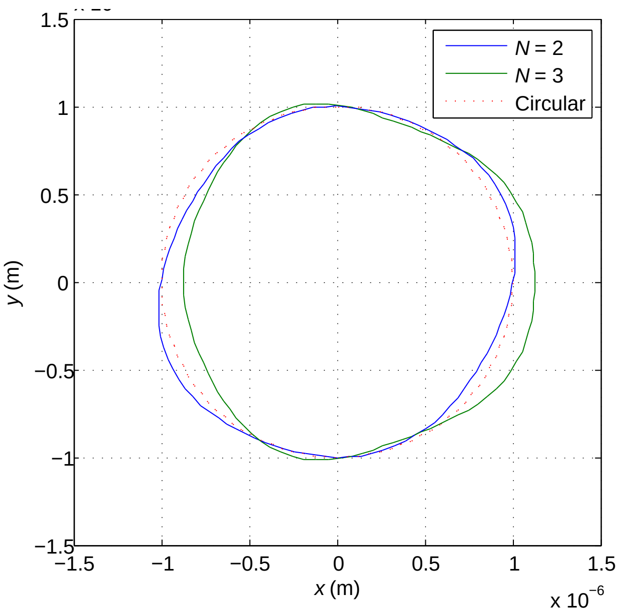

(a)

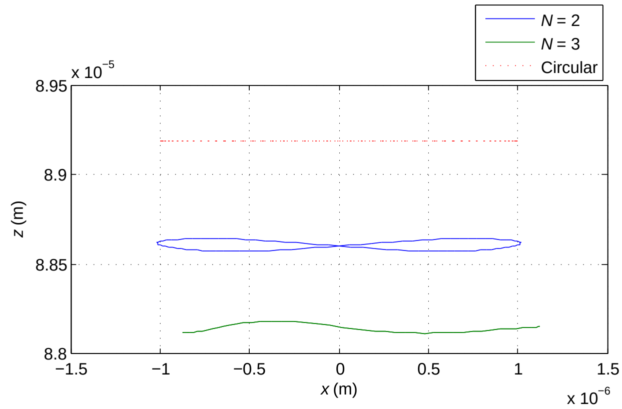

(b)

Figure 3.6: Final status of the vortex ring in front after 1 ms, with perturbation of constant amplitude-to-radius ratios A/R = 0.05 and $N = 2$ and 3, and compared to the final position of a circular ring of 1 μm radius in the (a) xy-plane and (b) xz-plane.

For b in the x-direction, the final radii plots of the perturbed cases display slight deviations from the circular case. They still possess the four typical regimes as the circular case does, but more impact parameters can lead to the production of two new rings from reconnection. The possibility for the two rings to merge into one large deformed loop is reduced.

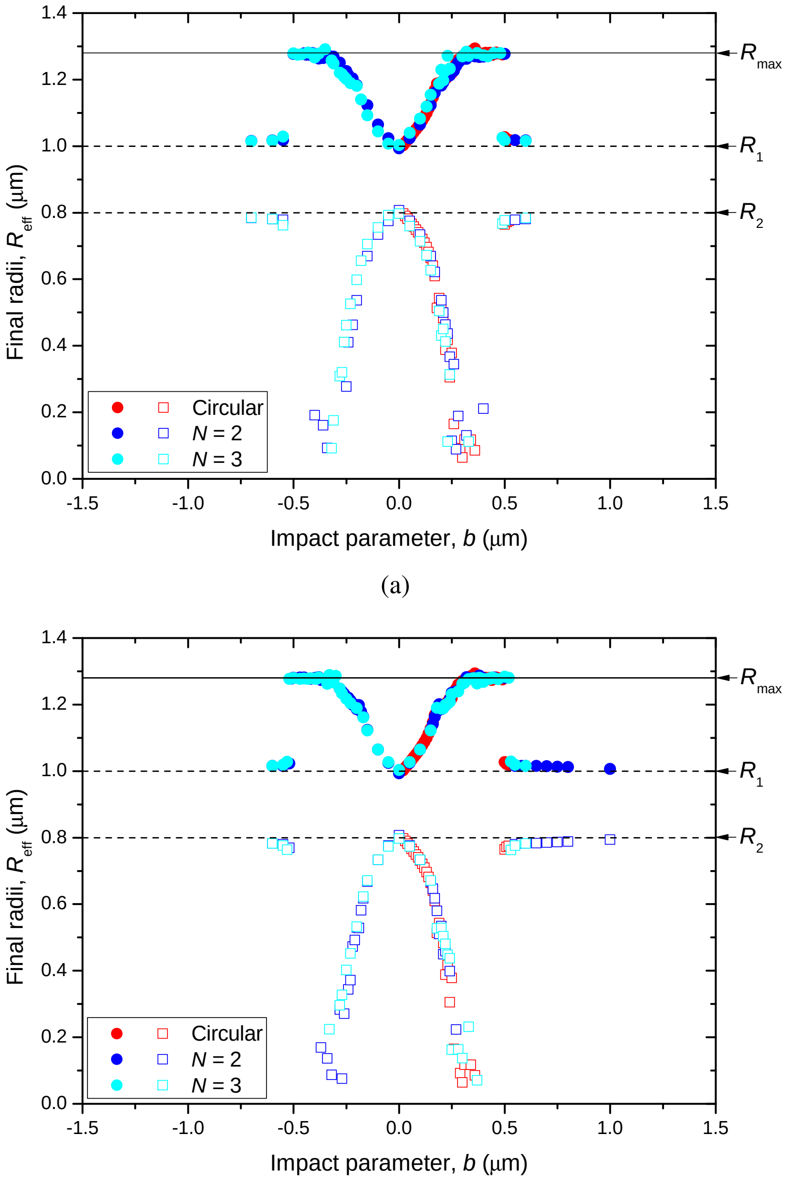

(a)

(b)

Figure 3.7: Final effective radii, $R_{\rm eff}$, for the first ring with manually imposed perturbation versus b varying in the (a) x-direction and (b) y-direction. The initial conditions include $R_1 = 1.0\,\mu$m and $R_2 = 0.8\,\mu$m, which are indicated by the dashed horizontal lines in plots, and $d = 5\,\mu$m. The solid symbol is for the larger ring and the open symbol is for the smaller one. Perturbation of $N = 2$ and 3 is imposed with the same amplitude $A/R = 0.05$. The maximum expected radius of the large loop formed by the merging of the initial vortex rings is $R_{\rm max} = \sqrt{R_1^2 + R_2^2} \approx 1.28\,\mu$m, indicated by the solid horizontal line.

3.4 Deformed Ring From Collision

In the previous sections, we investigated the interactions between two circular rings and between rings with manually imposed perturbation. However, these conditions are more ideal than the real experiments. In experiments, a pulse of vortex rings is fired into the cell in a very short duration. It is more likely that in a beam of many vortex rings, two rings reconnect and merge into one large and slow ring, which will then be hit by faster-moving small rings from behind. These secondary interactions possibly provide a better mechanism for small rings to be produced. This was simulated by shooting small circular rings into a large deformed ring created from the reconnection between two circular rings.

The initial setup for creating this deformed ring includes two circular rings with radii $R_1 = 1\,\mu$m, $R_2 = 0.8\,\mu$m, separated by $d = 3\,\mu$m, with impact parameter $b = 0.48\,\mu$m. As shown in Figure 3.8 (a), this ring is largely deformed compared to a circular ring with radius same as its effective radius $R_{\text{eff}} = 1.28\,\mu$m. The ring is strongly deformed from viewing in the xz-plane as shown in Figure 3.8 (b) as well. After the deformed loop has been formed and become stabilised in a few steps, another circular ring of radius $0.8\,\mu$m is added at $2\,\mu$m below. The asymmetric deformation of the large loop again requires the impact parameter to be varied in both x- and y-directions, and instead of the origin, this time $\boldsymbol{b} = (b_x, b_y)$ is varied with regard to the centre of the deformed ring.

The final radii R_{eff} with impact parameter being varied along both axes are plotted in Figure 3.9. The plots still possess some general features observed in the previous cases but their forms are very different not only between each other but also from the other cases. Now small rings are much easier to produce, and sometimes it is even possible to produce more than one small rings following one collision. On the rare occasion when there is only one large loop formed from the reconnection of the two

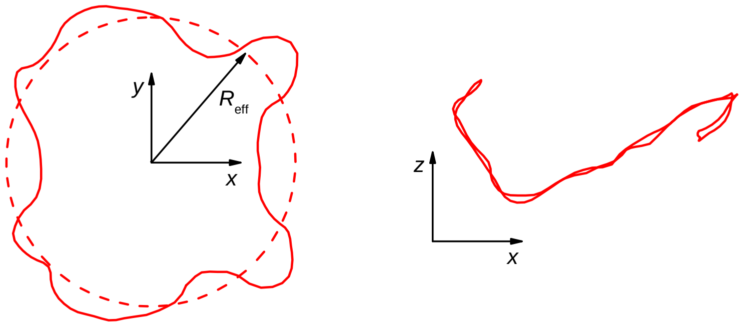

(a) (b)

Figure 3.8: The deformed ring created from colliding two circular rings seen in (a) xy-plane and (b) xz-plane, plotted in the same scale. The initial configurations for the circular rings are $R_1 = 1\,\mu$m at (0, 0, 3) μm and $R_2 = 0.8\,\mu$m at (0.48, 0, 0) μm. An equivalent circular ring of the same effective radius R_{eff} as the deformed ring is shown in dashed circle in (a).

rings, the loop often self-reconnects after some evolution in time and emits a small ring. It is highly unlikely to be left with only one single vortex ring. If we have some of these deformed loops created from ring collision in the experiment, it is probable to end up with quite a few small rings from the interactions with these secondary rings.

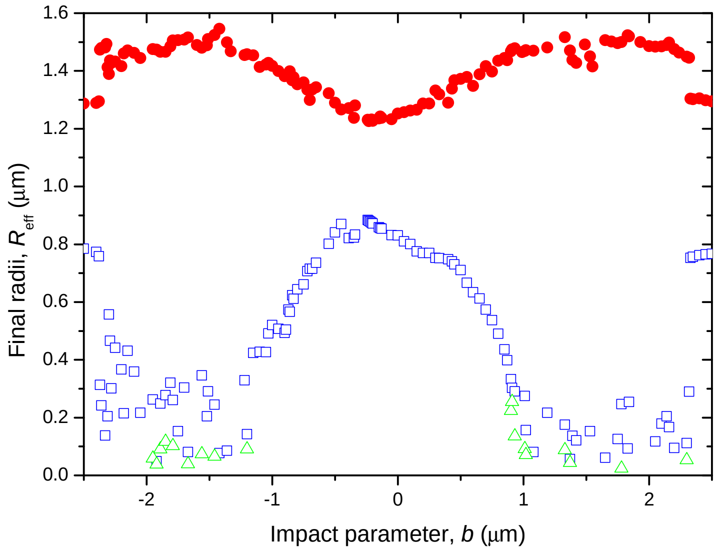

(a)

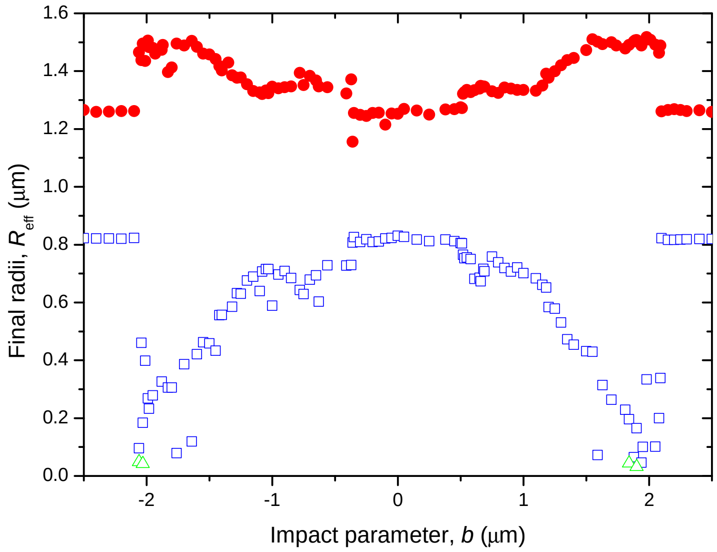

(b)

Figure 3.9: Final effective radii, R_{eff}, against varying b in the (a) x-direction and (b) y-direction. Initially, the first deformed ring as shown in Figure 3.8 is obtained from collision and a circular ring of radius 0.8 μm is placed 2 μm below the first one. The solid symbol is for the larger rings and the open symbol is for the smaller ones. The green triangles indicate the occurrence of more than one small rings.

Chapter 4

Dynamics of Charged Vortex Ring

4.1 Introduction

Charged vortex filaments have been used in experiments to study superfluid turbulence since Rayfield and Reif [46]. The dynamics of a charged circular ring in electric field is well known both experimentally and theoretically [20,54,55]. In recent experiments performed in Manchester [48] and in the experiments discussed in Chapter 2, vortex rings with an electron trapped in its core were injected into an electric field to probe superfluid turbulence. Although the rings are initially released due to reconnections at the surface of a large charged vortex tangle and are thus unlikely to be perfectly circular, the experimental time of flight agrees with the analytical calculation of a circular ring, providing that there are no ring-ring interactions. It is proposed that the electric field might have a smoothing effect on the rings and simulations of deformed vortex rings were run to test this theory.

In an early attempt to model the ion attached to a vortex ring, Samuels and Donnelly [55] found that despite the asymmetric location of the ion, it could cause a symmetric growth in ring radius and that the ring would be turned into rough alignment with the electric field. A simple model for the dynamics of the charged vortex filaments was implemented in our vortex filament program following the work by Tsubota and Adachi [54]. If a vortex ring with an ion of charge e and radius R_{ion} trapped by its core moves in a uniform electric field $\boldsymbol{E}$ in the zero temperature limit, an electric force acts on the charged part and we have

$$\frac{\mathrm{d}\boldsymbol{s}}{\mathrm{d}t} = \mathbf{v}_S + \frac{e}{2R_{\text{ion}}\rho_S\kappa}\boldsymbol{s}' \times \boldsymbol{E}, \tag{4.1}$$

where ρ_S is the superfluid density, $\mathbf{v}_S$ is the velocity of the superfluid component, R_{ion} is calculated as the average length of the neighbouring segments of the mesh point with charge and $\boldsymbol{s}$, $\boldsymbol{s}'$ refer to the coordinate of a point on the filament and its derivative. This equation does not account for the sliding motion of the ions along vortex lines [56] when $\boldsymbol{s}'$ can be parallel to the direction of the field $\boldsymbol{E}$. In the simulation performed by Tsubota and Adachi [54] of a perfectly circular vortex ring with a localised charge on one point, small-amplitude Kelvin waves excited by the electric field resulted in the expansion of the ring radius.

In our simulation, a singly charged vortex ring is placed in an unphysically high electric field with amplitude of 10^5 V/m such that the changes induced by the field can be more obvious in a very short amount of time. The ratio of the total line length to the effective circumference, $L/2\pi R_{\text{eff}}$, is possible to give us some idea on the amplitude of the deformation relative to the smoothed line length. This and the effective radius of the ring are monitored to see the effect of the field. We study the motion of a charged deformed ring created from ring collision in electric field in Section 4.2 and that of a charged ring with manually imposed perturbation in field in Section 4.3.

4.2 Deformed Ring From Collision

The same deformed ring created from ring collision used in Chapter 3 is chosen to be in this simulation. The initial conditions for creating this ring and its shape can be found in Figure 3.8. This ring originally has 131 mesh points and has an effective radius of 1.28 μm. Due to the asymmetric shape of the ring, we performed simulations with a charge imposed on a few different mesh points to validate the effect of the electric field on a localised charge.

An elementary charge e is placed on point 1, 30, 60, 90 or 120 of the deformed ring respectively. The change in the effective radius, R_{eff}, of the ring from 0 to 3 ms is plotted in Figure 4.1. The location of the charge does not have a huge impact on R_{eff}. The deformed ring expands quickly in the extremely large electric field to about 1.58 μm at 3 ms. The growth in size is over 20%. The amplitude of the Kelvin waves on the deformed ring is so large that on a few occasions, it is forced to self-reconnect and emit a small ring. The evolution of a circular ring with the same effective radius 1.28 μm and 131 mesh points is given in dashed curve. This circular ring expands even faster, to approximately 1.64 μm at the end of the simulation. From Equation 4.1, $\mathrm{d}\boldsymbol{s}/\mathrm{d}t$ is proportional to the cross product $\boldsymbol{s}' \times \boldsymbol{E}$. For a perfectly circular ring with velocity aligned in the direction of the electric field, $\boldsymbol{s}'$ is perpendicular to $\boldsymbol{E}$ at all time. But this is not always the case for a deformed ring. There can exist a component of $\boldsymbol{s}'$ that is parallel to $\boldsymbol{E}$, since a trapped ion is able to slide along a vortex filament to dissipate energy into Kelvin waves [56]. This ability of an ion to move along the vortex line is not accounted for in our model and thus the apparent suppression of the growth of the deformed ring is an artifact.

Now we look at the ratio $L/2\pi R_{\text{eff}}$ in Figure 4.2 to examine the variation of the ring deformation in the electric field. The field does induce some Kelvin waves on the singly-charged circular ring [54], but the amplitude of them is too small to be

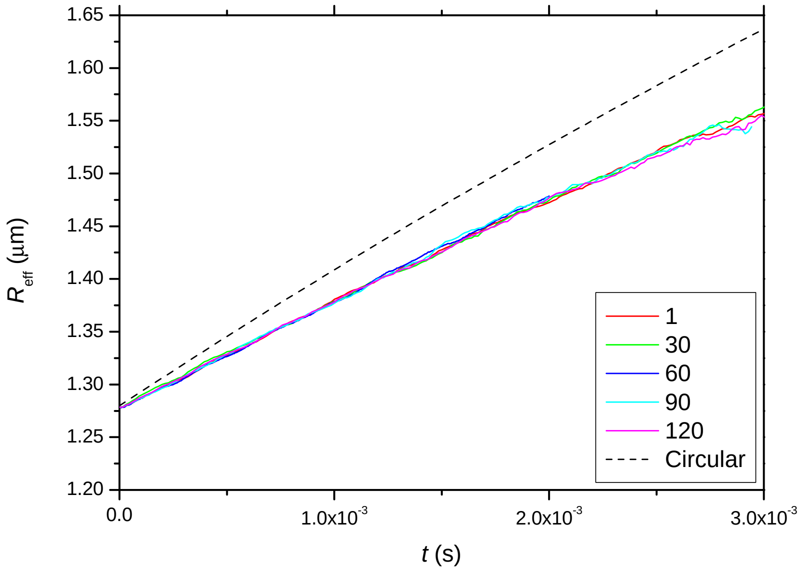

Figure 4.1: Evolution of the effective radius, R_{eff}, of the deformed ring with charge e imposed at 5 different mesh points (1, 30, 60, 90, 120). The dashed curve is for a circular ring with radius of $1.28\,\mu$m, same as the effective radius of the deformed ring, with charge e placed on the first mesh point.

resolved in our plot. $L/2\pi R_{\text{eff}}$ for the circular ring can be regarded as 1 throughout the time range, i.e., the ring remains circular to high accuracy. Without the charge, the deformed ring grows more distorted in time, which results in its self-reconnection at 2 ms and the emitting of a much smaller ring. However, when a charge is introduced, the deformation reduces in the electric field, proving that the field has a smoothing effect on charged vortex rings. The resemblance in the curves for charged deformed ring reaffirms the conclusion that the location of the charge is not important.

4.3 Manually Imposed Perturbation

The distortion on the ring created from collision is so strong that self-reconnection is almost unavoidable. A more controllable way of studying the dynamics of a charged deformed vortex ring is to use rings with manually imposed perturbation provided by

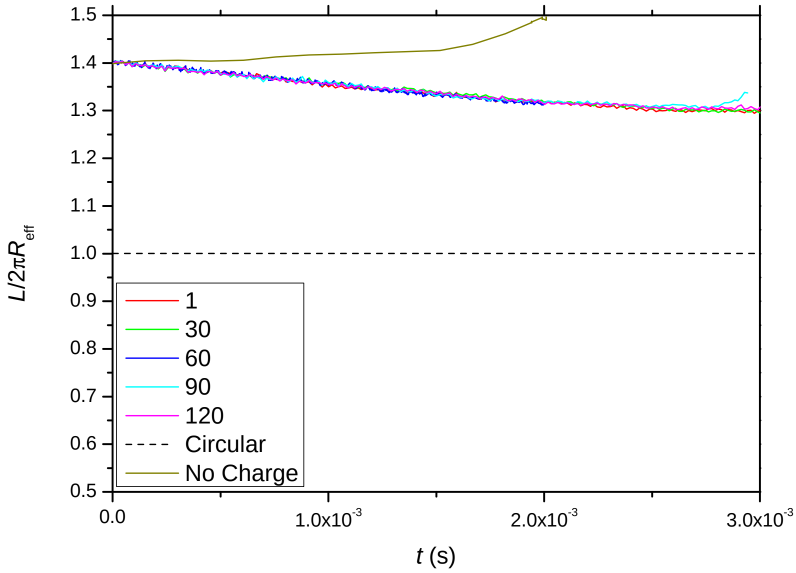

Figure 4.2: Ratio of total line length to the effective circumference, $L/2\pi R_{\text{eff}}$, of the deformed ring created from ring collision, with charge e imposed at 5 different mesh points. The dashed curve is for a circular ring with effective radius same as the deformed ring at 1.28 μm. Also plotted in dark yellow curve is the change in ratio for the deformed ring carrying no charge.

Equation 3.6, which proves to be more stable. The perturbation was applied on a circular ring with initial radius of 1 μm. The amplitude A and the number N were varied during the simulations. The electric field was kept at 10^5 V/m for more distinguishable results.

The vortex ring initially has a perturbation of constant amplitude $A/R = 0.05$ and $N = 1$, 2, 3 and 5. An elementary charge e is placed on the first mesh point. The plots are compared to the result for a singly-charged circular ring with the same initial radius of 1 μm. The effective radius plot is given in Figure 4.3. The curves are mostly indistinguishable for the rings with $N \leq 3$ from 0 to 0.04 s but the ring with $N = 5$ expands slightly faster in the field, which indicates that the number N helps with the growth in radius.

Figure 4.4 displays the ratio $L/2\pi R_{\text{eff}}$ of a singly-charged ring with perturbation of $N = 1$, 2, 3 and 5 from 0 to 0.04 s. The deformation on the ring reduces smoothly with a decreasing derivative in the electric field. The ring with $N = 5$ is the most deformed

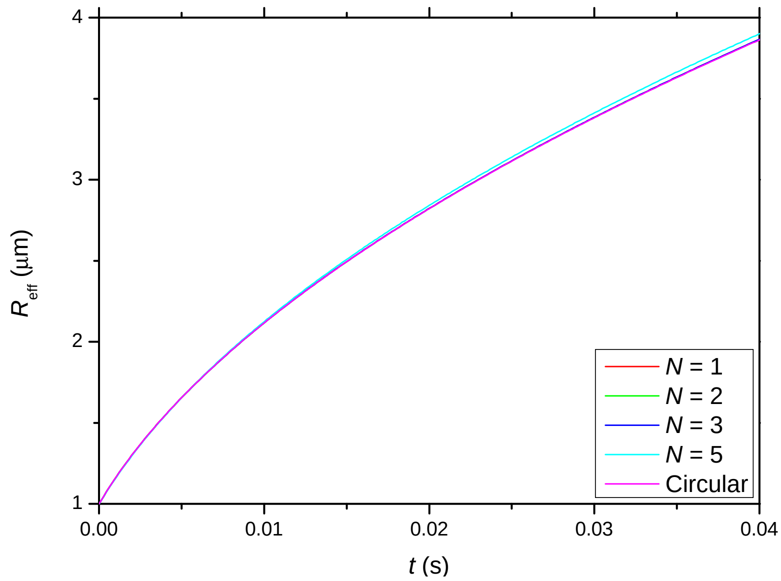

Figure 4.3: The effective radius, R_{eff}, of a charged vortex ring with perturbation of constant amplitude $A/R = 0.05$ and $N = 1$, 2, 3 and 5 from 0 to 0.04 s. The initial radius of the ring is 1.0 μm and R_{eff} of a singly-charged circular ring of the same size is plotted for comparison. One elementary charge e is placed on the first mesh point of the ring.

to begin with, but ends up with a $L/2\pi R_{\mathrm{eff}}$ value of 1.003, similar to that of the ring with $N = 3$ at 0.04 s.

Comparison between the projections of the deformed ring in the xy-plane before and after the simulation, i.e., at $t = 0$ and 0.04 s, is offered in Figure 4.5. The rings are aligned according to the positions of their centres. Perturbation of amplitude $A/R = 0.05$ and $N = 5$ is imposed on the ring. Apart from the growth in size, it is obvious that the initial ring in red is largely deformed with the perturbation but at the end of the simulation the ring in blue becomes much more circular. The large electric field has a strong smoothing effect on the ring.

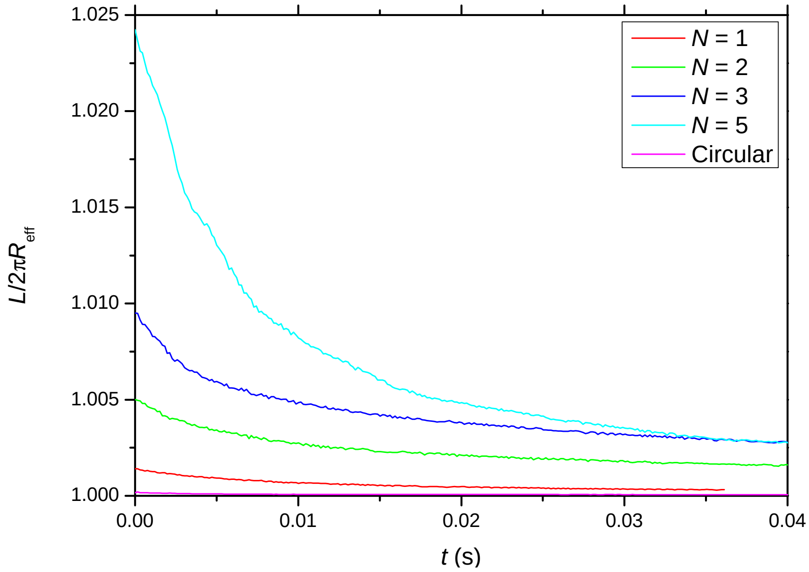

Figure 4.4: The ratio, $L/2\pi R_{\text{eff}}$, of a charged vortex ring with perturbation of constant amplitude $A/R = 0.05$ and $N = 1$, 2, 3 and 5, along with the ratio for a circular ring, from 0 s to 0.04 s. The initial radius of the ring is 1.0 μm. The first mesh point of the ring has charge e.

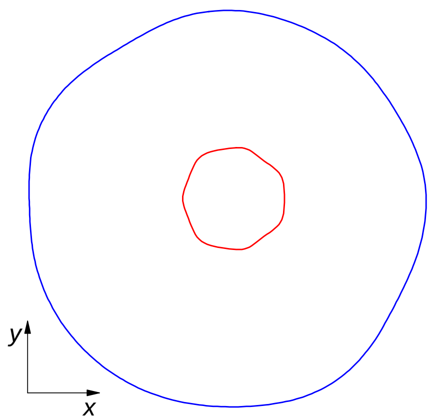

Figure 4.5: The projections of a deformed vortex ring in the xy-plane at $t = 0$ (red) and 0.04 s (blue), for a vortex ring with perturbation of $A/R = 0.05$ and $N = 5$. The rings are aligned according to the positions of their centres.

Chapter 5

Conclusions

The main purpose of this thesis is to study the dynamics of vortex rings in superfluid helium and how they interact with each other. This was achieved both experimentally and numerically.

We have analysed the data provided by the experiment performed at Manchester on charged vortex ring in superfluid ^{4}He. The experiment cell design was modified upon a previous version [45], in order to investigate the release of the charged vortex rings (CVRs) from the charged tangle near the injection tip and to observe the behaviours of the CVRs in a field-free region. Our analysis suggests that the release time and the initial size of the seed CVRs are almost constant and thus the properties of the charged tangle near the tip are neither voltage-dependent nor temperature dependent. It is also shown that the pulse length has limited impact on the experiments, except that more CVRs are injected into the cell when the pulse length is longer.

In the zero temperature limit, where the effect of mutual friction can be ignored, at low drive voltages below 50 V, the experimental time agrees with the analytical time of flight for an isolated CVR. As the drive voltage increases towards 200 V, the number of the reconnection events starts to rise, resulting in the early arrival of some secondary small rings and a wider spread of the radii of the CVRs. The formation of charged tangles is also expected with the reconnections, which serve as the dominant charge carriers at high voltages. When the temperature becomes higher, the mutual friction term is no longer negligible. Many of the CVRs are dissipated before reaching the top of the cell, leaving behind a stationary bare ion, and only large charged tangles have enough energy to finally reach the collector after some time.

The interactions between a pair of vortex rings initially travelling in the same direction in superfluid helium have been simulated employing the vortex filament method and the exact Biot-Savart law, for both circular and deformed rings. For two circular rings, depending on the impact parameters, four different scenarios can occur: the lower ring passes through the upper one without reconnecting; the lower ring clips the other one on the side, producing one larger and one smaller rings; the two rings merge into one large ring; the rings miss each other on the outside. The region for ring reconnection narrows if the difference in the initial radii reduces. The perturbation on the rings changes their interactions upon the same impact parameter. When a circular ring interacts with a deformed secondary large ring created by ring collision, there is a relatively large possibility of generating at least one small ring less than half of the size of the initial circular ring. Further insight could be provided if simulations on multiple interacting vortex rings are performed.

By constructing a model for the CVRs, it is shown that the electric field has a smoothing effect on the perturbation of the vortex rings, which explains why the rings behave like perfectly circular rings in the experiments even though they should be deformed after being released by reconnections in the charged tangle near the tip.

Bibliography

[1] P. Kapitza, Nature, **141**, 74 (1938).

[2] J. F. Allen, and A. D. Misener, Nature, **141**, 75 (1938).

[3] T. Guénault, *Basic Superfluids*, Taylor & Francis (2003).

[4] F. London, Nature, **141**, 643 (1938).

[5] L. Tisza, Nature **141**, 913 (1938).

[6] L. D. Landau, J. Phys. Moscow **5**, 71 (1941).

[7] E. Andronikashvili, J. Phys. U.S.S.R. **10**, 201 (1946).

[8] D. R. Tilley and J. Tilley, *Superfluidity And Superconductivity*, third edition, IOP (1990).

[9] L. Onsager, Nuovo Cimento Suppl. **6**, 279 (1949).

[10] W. F. Vinen, Proc. R. Soc. London A **260**, 218 (1961).

[11] P. G. Saffman and G. R. Baker, Ann. Rev. Fluid Mech. **11**, 95 (1979).

[12] R. P. Feynmann, Prog. Low Temp. Phys. **1** (1955).

[13] R. J. Donnelly, *Quantized Vortices in Helium II*, Cambridge University Press (1991).

[14] P. H. Roberts, R. J. Donnelley, Phys. Rev. **31A**, 137 (1970).

[15] G. W. Rayfield and F. Reif, Phys. Rev. **136**, A1194 (1964).

[16] C. L. M. H. Navier, Mém. Acad. Roy. Sci. **6**, 389-440 (1823).

[17] U. Frisch, *Turbulence*, Cambridge University Press, (1995).

[18] H. E. Hall and W. F. Vinen, Proc. R. Soc. London, Ser. A **238**, 204 (1956); **238**, 215 (1956).

[19] W. F. Vinen, Proc. R. Soc. London, Ser. A **240**, 114 (1957); **240**, 128 (1957); **242**, 493 (1957); **243**, 400 (1957).

[20] P. M. Walmsley, A. I. Golov, H. E. Hall, A. A. Levchenko, W. F. Vinen, Phys. Rev. Lett. **99**, 026502 (2007).

[21] P. M. Walmsley and A. I. Golov, Phys. Rev. Lett. **100**, 245301 (2008).

[22] K. W. Schwarz, Phys. Rev. B **31**, 5782 (1985); Phys. Rev. B **38**, 2398 (1988).

[23] R. J. Arms and F. R. Hama, Phys. Fluids **8**, 553 (1965).

[24] R. Hänninen and A. W. Baggaley, Proc. Natl. Acad. Sci. USA **111**, 4667 (2014).

[25] R. L. Ricca, D. C. Samuels, C. F. Barenghi, J. Fluid Mech. **391**, 29 (1999).

[26] V. L. Ginsburg and L. P. Pitaevskii, J. Phys. USSR **7**, 858 (1958).

[27] E. P. Gross, J. Math. Phys. **4**, 195 (1963).

[28] J. Koplik and H. Levine, Phys. Rev. Lett. **71**, 1375 (1993).

[29] R. M. Kerr, Phys. Rev. Lett. **106**, 224501 (2011).

[30] M. Kursa, K. Bajer, and T. Lipniacki, Phys. Rev. B **83**, 014515 (2011).

[31] W. F. Vinen, M. Tsubota, and A. Mitani, Phys. Rev. Lett. **91**, 135301 (2003).

[32] V. S. L'vov, S. Nazarenko, JETP Lett. **91**, 464 (2010).

[33] E. V. Kozik, B. V. Svistunov, Phys. Rev. B **77**, 060502(R) (2008); J. Low Temp. Phys. **156**, 215 (2009).

[34] A. W. Baggaley and J. Laurie, Phys. Rev. B **89**, 014504 (2014).

[35] A. W. Baggaley and C. F. Barenghi, Phys. Rev. B **83**, 134509 (2011).

[36] J. Koplik and H. Levine, Phys. Rev. Lett. **76**, 4745 (1996).

[37] M. Leadbeater, T. Winiecki, D. C. Samuels, C. F. Barenghi, and C. S. Adams, Phys. Rev. Lett. **86**, 1410 (2001).

[38] P. Chatelain, D. Kivotides, and A. Leonard, Phys. Rev. Lett. **90**, 054501 (2003).

[39] R. M. Caplan, J. D. Talley, R. Carretero-Gonzalez, and P. G. Kevrekidis, Phys. Fluids **26**, 097101 (2014).

[40] R. Hänninen, Phys. Rev. B **88**, 054511 (2013).

[41] D. Kivotides, J. C. Vassilicos, D. C. Samuels, and C. F. Barenghi, Phys. Rev. Lett. **86**, 3080 (2001).

[42] M. Leadbeater, D. C. Samuels, C. F. Barenghi, and C. S. Adams, Phys. Rev. A **67**, 015601 (2003).

[43] D. H. Wacks, A. W. Baggaley and C. F. Barenghi, Phys. Fluids. **26**, 027102 (2014).

[44] A. W. Baggaley, C. F. Barenghi and Y. A. Sergeev, Phys. Rev. E **89**, 013002 (2014).

[45] P. M. Walmsley, A. A. Levchenko, S. E. May, A. I. Golov, J. Low Temp. Phys. **146**, 511 (2007).

[46] G. W. Rayfield and F. Reif, Phys. Rev. **136**, A1194 (1964).

[47] V. B. Eltsov, R. de Graaf, R. Hänninen, M. Krusius, R. E. Solntsev, V. S. L'vov, A. I. Golov, P. M. Walmsley, Prog. Low Temp. Phys. **16**, 46 (2009).

[48] P. M. Walmsley, P. A. Tompsett, D. E. Zmeev, and A. I. Golov, Phys. Rev. Lett. **113**, 125302 (2014).

[49] A. I. Golov, P. M. Walmsley, P. A. Tompsett, J. Low Temp. Phys. **161**, 509 (2010).

[50] A. W. Baggaley, J. Low Temp. Phys. **168**, 18 (2012).

[51] R. Hänninen, A. W. Baggaley, Proc. Natl. Acad. Sci. USA **111**, 4667 (2014).

[52] P. G. Saffman, *Vortex Dynamics*, Cambridge University Press (1992).

[53] C. F. Barenghi, R. Hänninen and M. Tsubota, Phys. Rev. E **74**, 046303 (2006).

[54] M. Tsubota, H. Adachi, J. Low Temp. Phys. **158**, 364 (2010).

[55] D. C. Samuels and R. J. Donnelly, Phys. Rev. Lett. **67**, 2505 (1991).

[56] R. M. Ostermeier, W. I. Glaberson, J. Low Temp. Phys. **25**, 317 (1976).